Mapping and reprogramming microenvironment-induced cell states in human disease using generative AI

Amir Akbarnejad[1,2+], Lloyd Steele[1,3+], Daniyal J. Jafree[1,4+], Sebastian Birk[1,5,6+], Marta Rosa Sallese[1,7,8,9+], Koen Rademaker[1], Adam Boxall[1], Benjamin Rumney[1], Catherine Tudor[1], Minal Patel[1], Martin Prete[1], Stanislaw Makarchuk[1], Tong Li[1], Heather Stanley[1], April Rose Foster[1], Kenny Roberts[1], Andrew L. Trinh[1], Carlo Emanuele Villa[9], Giuseppe Testa[7,8,9], Satveer Mahil[10], Arash Mehrjou[11], Catherine Smith[12], Sattar Vakili[13], Menna R. Clatworthy[1,14], Thomas Mitchell[15], Omer Ali Bayraktar[1], Muzlifah Haniffa[1,16,17]*, Mohammad Lotfollahi[1,2,12]*

[1] Wellcome Sanger Institute, Wellcome Genome Campus, Hinxton, UK
[2] Cambridge Center for AI in Medicine, University of Cambridge, Cambridge, UK
[3] Trinity College, University of Cambridge, Cambridge, UK
[4] UCL Great Ormond Street Institute of Child Health, University College London, London, UK
[5] School of Computation, Information and Technology, Technical University of Munich, Munich, Germany
[6] Institute of AI for Health, Helmholtz Center Munich – German Research Center for Environmental Health, Neuherberg, Germany
[7] Department of Experimental Oncology, European Institute of Oncology IRCCS, Milan, Italy
[8] Department of Oncology and Hemato-Oncology, University of Milan, Milan, Italy
[9] Human Technopole, Milan, Italy
[10] St John's Institute of Dermatology, King's College London and Guy's & St Thomas' NHS Foundation Trust, London, UK
[11] GSK.ai
[12] Cambridge Stem Cell Institute, University of Cambridge, Cambridge, UK
[13] Mediatek Research, Cambridge, UK
[14] Tissue Immunity Group, MRC Laboratory for Molecular Biology, Cambridge, UK
[15] Early Cancer Institute, University of Cambridge, UK
[16] Department of Dermatology and NIHR Newcastle Biomedical Research Centre, Newcastle, UK
[17] CIFAR Macmillan Multi-scale Human Program, CIFAR, Toronto, Ontario, Canada

+ Shared first authors
* Joint corresponding authors. Address correspondence to
mh32@sanger.ac.uk; ml19@sanger.ac.uk

Abstract

Tissue microenvironments reprogram local cellular states in disease, yet current computational spatial methods remain descriptive and do not simulate tissue perturbation. We present MintFlow, a generative AI algorithm that learns how the tissue microenvironment influences cell states and predicts how tissue perturbations can change and reprogram them. Applied to three human diseases, MintFlow uncovered distinct pathogenic spatial reprogramming in inflammatory and tumor microenvironments. In atopic dermatitis, MintFlow prioritized an epidermal resident T cell program and a dendritic cell activation niche within inflammatory hotspots within the superficial dermis. In melanoma, MintFlow identified fibrotic stroma resembling keloid scar tissue. In kidney cancer, MintFlow resolved immunosuppressive $CD8^+$ T cell states within tertiary lymphoid structures. Furthermore, MintFlow enabled *in silico* perturbations of disease-relevant cell states and tissue environments. Regulatory T cell modulation in atopic dermatitis suppressed the pro-inflammatory tissue environment, supporting manipulation of these cells as a therapeutic target. Spatially-targeted macrophage depletion in kidney cancer reverted immunosuppressed T cell states, and the corresponding gene programs correlated with survival in large kidney cancer patient cohorts. These findings position MintFlow as a tool for unbiased prediction of disease mechanisms and *in silico* perturbations to accelerate translational hypothesis generation and guide therapeutic strategies.

Introduction

Recent advances in single-cell and spatial transcriptomics are reshaping biomedical research by enabling the dissection of tissue architecture and cell identity with unprecedented resolution. These technologies allow researchers to map how specific cell types, transcriptional programs, and cellular interactions contribute to health and disease in their native spatial contexts. Such spatially resolved insights are expected to inform next-generation diagnostics, uncover context-specific therapeutic targets, and support the design of precision therapies including immunotherapies and regenerative strategies[1]. Understanding how cellular behavior is shaped within intact tissues is especially critical in complex and multifactorial diseases, where pathological outcomes often arise not only from changes within individual cells, but also from disrupted interactions between cells and their surrounding microenvironment. For instance, spatially restricted immunosuppressive signaling networks in tumors can drive immune evasion and resistance to therapy[2,3], spatial gradients of chemokines can sustain chronic inflammation in skin diseases such as atopic dermatitis (AD)[4], and localized glial–neuronal signaling has been implicated in the propagation of neuroinflammation in Alzheimer's disease[5]. A key challenge to understanding these diseased tissue ecosystems is to distinguish intrinsic gene programs that define cellular identity from the external signals induced by each cell's surrounding microenvironment.

Computational approaches to resolve cell-intrinsic from microenvironment-induced signals coupled with the ability to perform *in silico* perturbations to model and virtually reprogram tissue ecosystems would mark a paradigm shift in biomedical discovery. These opportunities move beyond existing descriptive analyses of pathological states, towards predicting disease mechanisms and potential targets to revert disease states. Such capabilities would not only aid the identification of cellular drivers of disease, but also support patient stratification, prognostic modeling, and the prioritization of therapeutic targets based on their spatial and contextual effects. Existing computational methods to model the effect of tissue microenvironment either overlook disentangling intrinsic and microenvironment-induced variation[6–9], lack mechanistic interpretability and require post-hoc interpretation of embeddings[6,10,11], are not flexible due to linear assumptions[12–14], do not scale well[10,13,14], or require prior knowledge about gene-gene interactions[15–17] (detailed comparison in Supplementary Note 1). Furthermore, existing methods fall short in prioritizing microenvironments and genes to make novel biological hypotheses, and in enabling in silico perturbations to test those hypotheses or generate new ones. Crucially, filling the latter gap enables hypothesis-driven, context-aware precision medicine via in silico perturbations and biological hypotheses generation.

To address the unmet need for modeling how the tissue microenvironment shapes cell identity and clinical outcomes, we present MintFlow, a generative AI framework based on flow matching (Fig. 1 and Methods) with theoretically grounded solution (identifiability proof in Methods and Supplementary Note 2) that disentangles intrinsic from microenvironment-induced gene expression in spatial transcriptomics data. Without relying on prior knowledge, predefined domains, or ligand–receptor pairs, MintFlow learns microenvironment-induced gene programs (MGP) at single-cell resolution and enables *in silico* perturbation of the tissue microenvironment, simulating how changes in local cellular context alter gene expression. Applied across spatial datasets from atopic dermatitis (AD), melanoma, and renal cell carcinoma (RCC), MintFlow uncovered spatially organized, disease-specific cell states. In atopic dermatitis, Mintflow identified microenvironment-induced epidermal resident memory T (T_{RM}) cells. *In silico* perturbation of skin microenvironments revealed cellular therapy with regulatory T cells (Tregs) as a potentially valuable therapeutic strategy. In melanoma, MintFlow identified fibrotic immune-excluding stroma and angiogenic tumor progenitors; and in RCC, simulated macrophage depletion reprogrammed exhausted T cell states and stratified survival in large cohorts. These findings position MintFlow as a generative AI model for uncovering spatially encoded drivers of disease and virtually modelling microenvironmental interventions, surmounting the challenge of recreating these features using *in vitro* and *in vivo* models. We envision MintFlow as a step toward AI-driven construction of virtual tissue models, accelerating the discovery of spatial biomarkers, guiding therapeutic design and, ultimately, improving the clinical translation of spatial biology for patient care.

Results

MintFlow learns microenvironment-induced cell states and predicts tissue perturbations

We designed MintFlow, a deep generative model that learns the effects of spatial context on a cell's gene expression by explicitly modeling incoming and outgoing cellular communication signals for a specific cell as latent variables. MintFlow learns to generate disentangled gene expression data driven by intrinsic variability and spatial context, respectively, enabling identification of cell states that are influenced by their microenvironment. By learning a joint representation of each cell's intrinsic identity and its tissue context, MintFlow provides a comprehensive understanding of how the local tissue environment reprograms cellular behavior (Fig. 1a–c, Methods).

In addition to disentangling intrinsic and microenvironment-induced effects, MintFlow introduces the concept of tissue perturbation. By simulating changes in the environment, MintFlow predicts how these alterations influence gene expression at scale. Through *in silico* perturbation, MintFlow models the outcomes of cell deletion or replacement within a tissue, offering valuable insights into how microenvironmental shifts impact gene expression. This capability enables large-scale hypothesis generation and testing, providing new avenues for exploring the dynamic interplay between cells and their surrounding environments.

MintFlow encodes each cell using the gene expression and cell type label of the cell itself, as well as those of cells within the local tissue microenvironment. Precisely, a multi-stage encoder learns a cell's intrinsic latent features, conditioned on the cell's cell type label, and microenvironment-induced latent features, conditioned on the composition of cells within its tissue microenvironment (i.e. its microenvironment cell type composition (MCC). These latent features are decoded into corresponding gene expression vectors: x_n^{int} and x_n^{mic}, respectively using flow matching (Methods). The sum of these expression vectors reconstructs the original expression vector.

MintFlow decomposition enables multiple downstream applications. Clustering the microenvironment-induced latent features captures fine-grained microenvironment-induced cell states (MCS; Fig. 1d and Methods). Moreover, it enables the calculation of a "microenvironment score", quantifying the relative influence of microenvironment signals on each cell to identify spatial hotspots of signaling activity (Fig. 1d and Methods). The microenvironment-induced gene expression can be analyzed with standard single-cell software such as scanpy[18] to derive differentially expressed genes and identify microenvironment-induced gene programs (MGPs) (Fig. 1e). Additionally, MintFlow enables *in silico* tissue perturbation simulating deletion or replacement of any cell within a tissue microenvironment, and predicts the resultant gene expression following perturbation, enabling large scale hypotheses generation and evaluation (Fig. 1f).

We benchmarked MintFlow's capability to predict microenvironment-induced gene expression against alternative methods and random baselines on simulated data. For the latter, we simulated known microenvironment-induced effects to provide ground truth to evaluate model performance (Supplementary Fig. 1 and Methods). MintFlow significantly outperformed alternatives in predicting microenvironment-induced gene expression based on three different metrics (Fig. 1g, Supplementary Figs. 2 and 3 and Methods). We also compared MintFlow's performance on real data, including single-sample Xenium data from one tissue section of AD and melanoma, respectively, and a multi-sample Xenium dataset of ten AD tissue sections (Fig. 1h and Methods). MintFlow proportions of microenvironment-induced read counts were on average higher in previously reported signaling genes[19] compared to other genes. In contrast, alternative methods either assigned more signaling gene read counts to intrinsic expression relative to microenvironment-induced expression, or only assigned a tiny proportion of the read counts to microenvironment-induced expression.

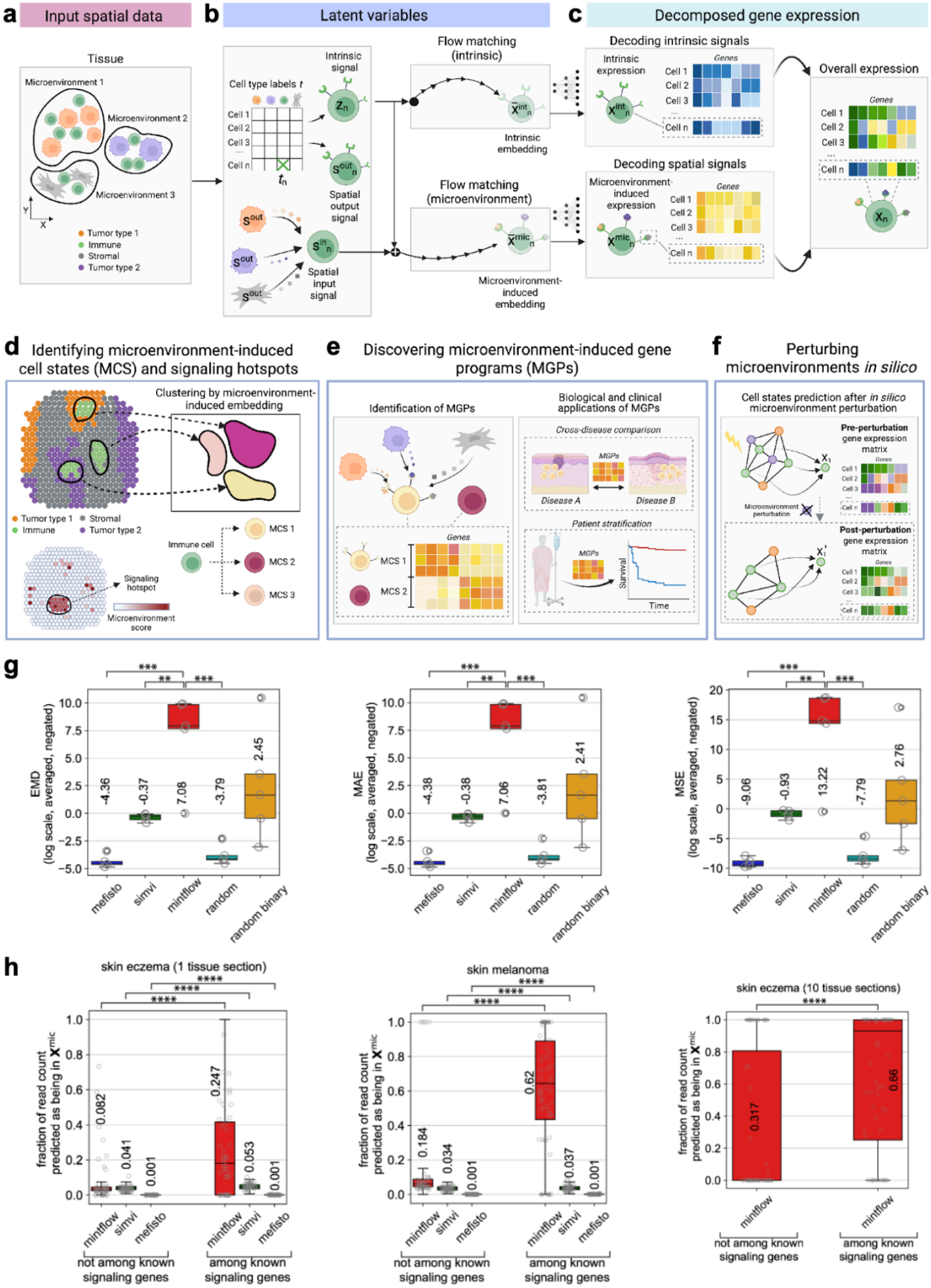
a
Input spatial data
Tissue
Microenvironment 1
Microenvironment 2
Microenvironment 3
Tumor type 1
Immune
Stromal
Tumor type 2
b
Latent variables
Cell type labels t
Intrinsic signal
Spatial output signal
Spatial input signal
Flow matching (intrinsic)
Intrinsic embedding
Flow matching (microenvironment)
Microenvironment-induced embedding
c
Decomposed gene expression
Decoding intrinsic signals
Intrinsic expression
Genes
Cell 1
Cell 2
Cell 3
Cell n
Decoding spatial signals
Microenvironment-induced expression
Overall expression
d
Identifying microenvironment-induced cell states (MCS) and signaling hotspots
Clustering by microenvironment-induced embedding
Tumor type 1
Stromal
Immune
Tumor type 2
Immune cell
MCS 1
MCS 2
MCS 3
Signaling hotspot
Microenvironment score
e
Discovering microenvironment-induced gene programs (MGPs)
Identification of MGPs
Biological and clinical applications of MGPs
Cross-disease comparison
MGPs
Disease A
Disease B
Patient stratification
Survival
Time
f
Perturbing microenvironments in silico
Cell states prediction after in silico microenvironment perturbation
Pre-perturbation gene expression matrix
Microenvironment perturbation
Post-perturbation gene expression matrix
g
EMD (log scale, averaged, negated)
MAE (log scale, averaged, negated)
MSE (log scale, averaged, negated)
mefisto
simvi
mintflow
random
random binary
h
skin eczema (1 tissue section)
skin melanoma
skin eczema (10 tissue sections)
fraction of read count predicted as being in X^mic
not among known signaling genes
among known signaling genes

Fig. 1 | Overview and benchmarking of MintFlow. a, Given one or multiple tissue sections, MintFlow determines each cell's microenvironment (Methods). MintFlow requires cell type labels as supervision and computes each cell's microenvironment cell type composition (MCC). **b**, MintFlow infers three embedding vectors that encode the intrinsic (z_n), the incoming spatial signals (s_n^{in}) that contribute to a cell's transcriptome, and the outgoing spatial signals (s_n^{out}) that a cell sends to its microenvironment. z_n and s_n^{out} are generated with priors conditioned on the cell's cell type label, while s_n^{in} is an aggregation of the outgoing spatial signals of the cell's microenvironment (s^{out}). Using flow matching, z_n and s_n^{in} are transformed into the intrinsic ($\bar{x}_n^{int}$) and microenvironment-induced ($\bar{x}_n^{mic}$) embeddings, which are decoded to generate intrinsic and microenvironment-induced read count vectors, respectively. These two components are added to reconstruct the original read count vector. **d**, Clustering MintFlow's microenvironment-induced embeddings enables fine-grained separation of cell types by microenvironment-induced cell states (MCS). A microenvironment score highlights signaling hotspots (Methods). **e**, Users can leverage MintFlow's inferred microenvironment-induced cell states and gene expression to identify microenvironment-induced gene programs (MGPs), comparing between conditions and stratifying patients. **f**, MintFlow enables to analyze the effects on cell states and MGPs after perturbing microenvironments. **g**, MintFlow outperforms alternative methods in read count disentanglement on simulated data. MAE, mean absolute error; EMD, earth mover's distance; MSE, mean squared error. All metrics are negated such that higher values are better. **h**, On real data, MintFlow is more likely to assign read counts of previously reported signaling genes to the microenvironment-induced component compared to alternative methods (Methods). Counts < 20 were filtered. Boxplot elements are defined as center line, median; box limits, upper and lower quartiles; whiskers, 1.5× interquartile range. Four, three, two, and one asterisks respectively indicate p-values less than or equal to 0.0001, 0.001, 0.01, and 0.05 in a t-test.

MintFlow identifies a microenvironment-induced T_{RM} cell state and T cell activation hub in atopic dermatitis

We first applied MintFlow on a dataset of 10 human skin tissue sections from 8 individuals with atopic dermatitis profiled by Xenium 5k, including 8 newly generated sections (Methods). Atopic dermatitis, a chronic inflammatory skin disease, is characterized by type 2 inflammation[4]. We included both inflamed (lesional) and phenotypically normal (non-lesional) skin samples. After quality control (Methods), we obtained 197 487 cells.

MintFlow identified regions with high microenvironment scores, consistent with high signaling activity, in the superficial dermis of the skin (Fig. 2a). These regions correlated with perivascular inflammatory infiltrate on H&E (Fig. 2a), which is a histopathological feature of disease. To further understand these regions, we clustered microenvironment-induced gene expression to

identify 10 distinct microenvironment domains in the skin across samples (Fig. 2b, Supplementary Fig. 4a and Methods). The *T_DC* domain was prominent in the superficial dermis, where high microenvironment scores were evident (Fig. 2b). The *T_DC* domain was formed of predominantly T cells, as well as antigen-presenting cells (APCs) such as migratory dendritic cells (MigDCs) and type 2 conventional dendritic cells (cDC2) (Supplementary Fig. 4b). The *T_DC* domain was also expanded in inflamed skin compared to non-inflamed skin (Fig. 2c), suggesting a potential pathogenic role.

We used MintFlow to derive MGPs for each microenvironment domain. The *T_DC* MGP included genes involved in T cell activation and homing (*ITGB2*, *SELPLG*)[20], T cell interactions with APCs (*ICAM3, ITGAL* (encodes LFA-1))[21,22], type 2 immunity polarization (*IL21R, ALOX15*)[23], and chemotactic positioning of immune cells (*CCL22, CCL19*) (Fig. 2d). We performed cell-cell communication analysis using chemokines in the *T_DC* MGP (*CCL19*, *CCL22*) to further understand interactions using atopic dermatitis scRNA-seq data[24]. This analysis highlighted a CCL19/CCR7 axis in which *F3: FRC-like* fibroblasts recruit *MigDCs* and *T* cells, as previously reported in skin[25], as well as a *CCL22-CCR4* axis for *MigDC-T* interactions (Fig. 2d and Supplementary Fig. 4c). Importantly, *MigDC-T* cell interactions are crucial to generating immune responses. Pathway analysis using the *T_DC* MGP showed also highest enrichment for a T cell activation process (Supplementary Fig. 4d and Methods), suggesting that the *T_DC* domain represented a T cell activation hub for type 2 immunity.

Identification of the *T_DC* domain by MintFlow enabled us to query potential new drug targets using a computational pipeline to predict drug targets (drug2cell)[26]. This analysis correctly identified drugs with known efficacy in atopic dermatitis (upadacitinib (a Janus kinase (JAK) inhibitor), prednisolone (a glucocorticoid))[27], in addition to potentially novel drugs (Fig. 2e and Supplementary Fig. 4e). For example, Amlexanox is used for treating aphthous ulcers, but with evidence for a PDE4 inhibitor action[28]. PDE4 inhibition is an FDA approved topical therapy for atopic dermatitis[29].

Next, we sought to (1) validate the *T_DC* MGP in external single-cell RNA sequencing (scRNA-seq)[24] in atopic dermatitis, and (2) investigate its cross-tissue relevance using a dataset of 23 different diseases across 6 human tissues that we previously integrated[25]. For scRNA-seq data, we used an independent cohort of 4 patients with atopic dermatitis[24]. We identified that inflamed/lesional samples demonstrated higher expression of the *T_DC* MGP compared to non-inflamed skin (Supplementary Fig. 4f and Methods). For the cross-tissue comparison across human diseases (Fig. 2d and Methods), we identified the highest *T_DC* MGP score in eosinophilic chronic rhinosinusitis with nasal polyps (CRSwNP). This was a notable finding as CRSwNP is a disease of type 2 immunity affecting the nasal mucosa, and dupilumab, a monoclonal antibody targeting IL-4 and IL-13 type 2 immunity signaling, is efficacious in both atopic dermatitis and eosinophilic CRSwNP[30]. We also identified high scores for inflammatory bowel disease (IBD) and psoriatic arthritis, which can be treated with JAK inhibitors. This

suggests a role for the *T_DC* domain in T cell activation across tissues, potentially reflecting similar lymphoid-like follicular niche structures across human inflammatory diseases[31].

Given the role of T cells in atopic dermatitis pathology and the *T_DC* domain[29], we next used MintFlow to disentangle T cell gene expression into microenvironment-induced and intrinsic factors. For the intrinsic latent space, we identified distinct clusters for naive (*CCR7*, *SELL*) and regulatory (*FOXP3*, *TIGIT*, *CTLA4*) genes (Fig. 2f). These cell clusters did not demonstrate a clear spatial pattern (Fig. 2g). In contrast, clustering T cells by microenvironment-induced gene expression revealed a transcriptionally distinct *CD8A*+*ITGAE*+*GZMB*+ T cell cluster associated with increased expression of *IL13*, *IL22*, and *GZMB* that was located in superficial skin (Fig. 2h,i). Transcriptomically and spatially, this T cell phenotype was characteristic of epidermal T_{RM}[32], which are known to have a spatially-imprinted phenotype across human tissues[33]. A CRISPR knockout mouse study recently validated *ITGAE* and *GZMB* as spatially imprinted genes in CD8+ T cells in superficial intestinal tissue[34], suggesting that Mintflow correctly identified a microenvironment-induced pathogenic T cell state in atopic dermatitis skin.

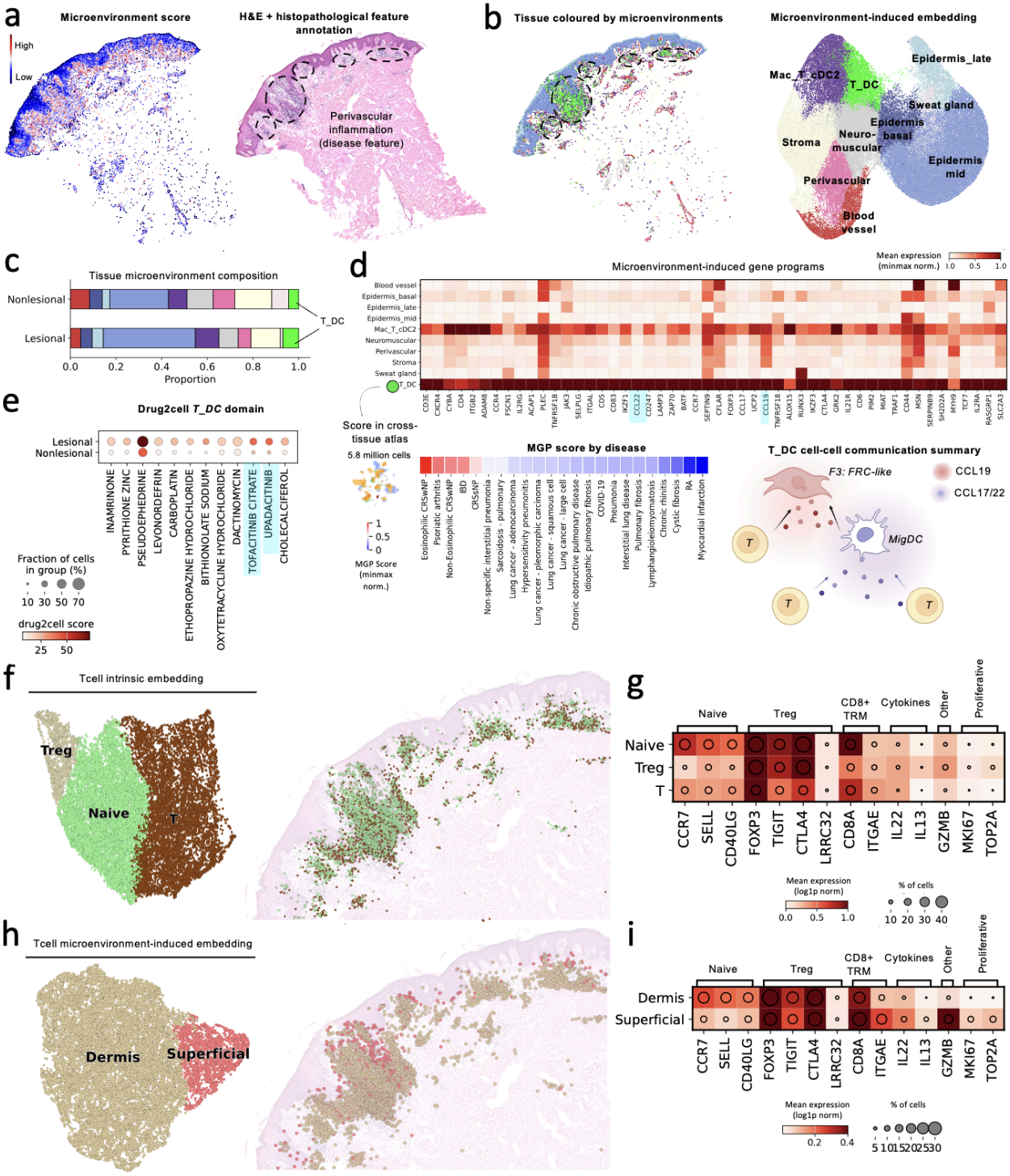

Fig. 2 | MintFlow identifies a microenvironment-induced T_{RM} cell state and T cell activation hub in atopic dermatitis. a, Tissue section colored by microenvironment score and haematoxylin & eosin (H&E) slide with annotated histopathological features of the same tissue section profiled by Xenium 5k. **b**, Tissue section colored by microenvironment clusters and UMAP visualization of microenvironment-induced embedding. **c**, Tissue composition by

microenvironment domains in inflamed and non-inflamed skin. **d**, MGP for *T_DC* domain and gene module scores of the *T_DC* MGP in a cross-tissue atlas (Methods). MGP, microenvironment-induced gene program. **e**, Drug2cell results for genes in the *T_DC* domain for all drugs. **f**, UMAP visualization of intrinsic expression matrix for T cells (left) and location of cells in inflamed tissue (right). **g**, Combined heatmap and dotplot for selected T cell markers for intrinsic clusters. **h**, UMAP visualization of microenvironment-induced expression matrix for T cells (left) and location of cells in inflamed tissue (right). **i**, Combined heatmap and dotplot for selected T cell markers for microenvironment-induced clusters.

In silico spatial perturbations model cellular therapy in atopic dermatitis

We next used MintFlow to perform *in silico* spatial perturbation of the *T_DC* MGP in the inflamed atopic dermatitis skin microenvironment. We performed *in silico* depletion/augmentation of Tregs as their specific role in atopic dermatitis is unclear and Treg modulation is being actively explored as a cellular therapy in immune-mediated diseases[35,36]. In the first perturbation, we removed Tregs from the microenvironment (Treg depletion). In the second perturbation, we replaced all T_{conv} cells (i.e. other T populations) with Tregs (Treg augmentation). We performed each perturbation in the same tissue region (Fig. 3a) and assessed the impact on immune cells within the tissue microenvironment (T_{conv} cells and MigDCs) using differential gene expression testing and pathway analysis (Methods).

When Tregs were removed from the microenvironment (Fig. 3b,c), MigDCs upregulated genes involved in inflammatory response (rank 1), regulation of MAPK cascade (rank 2), and cytokine-mediated signaling pathways (rank 9) (Fig. 3d). Interestingly, MAPK is important for DC activation and chemotaxis[37]. T_{conv} cells upregulated genes involved in lymphocyte chemotaxis and migration, as well as eosinophil chemotaxis - a cell type associated with active type 2 inflammation (Fig. 3d)[29,30]. One of the top 5 DEGs in MigDCs was the chemokine *CCL22* (Supplementary Figure 5a), which we had previously identified in the *T_DC* MGP (Fig. 2d). Overall, the *in silico* perturbation of Treg depletion suggested an increased inflammatory state with eosinophil and T cell infiltration, and thus likely a worsened atopic dermatitis phenotype. In agreement with this predicted effect, individuals with Treg dysfunction *in vivo* develop severe atopic dermatitis due to hyperinflammatory T cells in IPEX (immune dysregulation, polyendocrinopathy, enteropathy, X-linked) syndrome[38].

Next, we investigated the effect of Treg augmentation by replacing all T_{conv} cells with Tregs (Fig. 3e). In this setting, we did not observe enriched inflammatory pathways in MigDCs (Fig. 3f and Supplementary Fig. 5b). Instead, the top biological process related to receptor internalization. This suggested that MintFlow correctly predicted pro-inflammatory effects in Treg depletion and their absence in Treg augmentation.

We next queried whether Mintflow could predict the direction of change in expression of genes linked to active inflammation in MigDCs. In addition to chemokines secreted by MigDCs (*CCL17*, *CCL22*), we assessed migration/maturation markers (*CCR7*, *LAMP3*, *CD274, EBI3*)[39]

and type 2 immunity-related genes (*MMP12, ALOX15*)[4,40] (Fig. 3g). We observed that in Treg depletion (perturbation 1), these genes were increased, consistent with an active inflammatory state (Fig. 3g). *CCR7* is the receptor to *CCL19*, suggesting increased homing to perivascular lymphoid regions (Fig. 3h). *CCL22* is reported to facilitate T reg-MigDC interactions in lymphoid tissues[41]. In the Treg augmentation perturbation, these migration and type 2 immunity-related markers were downregulated (Fig. 3g).

Overall, our findings support the hypothesis that Treg modulation may be a potentially valuable therapeutic strategy in AD. Treg cellular therapy is being actively explored in other immune-mediated diseases such as IBD, with proof-of-concept that Treg therapies reverse disease activity[38].

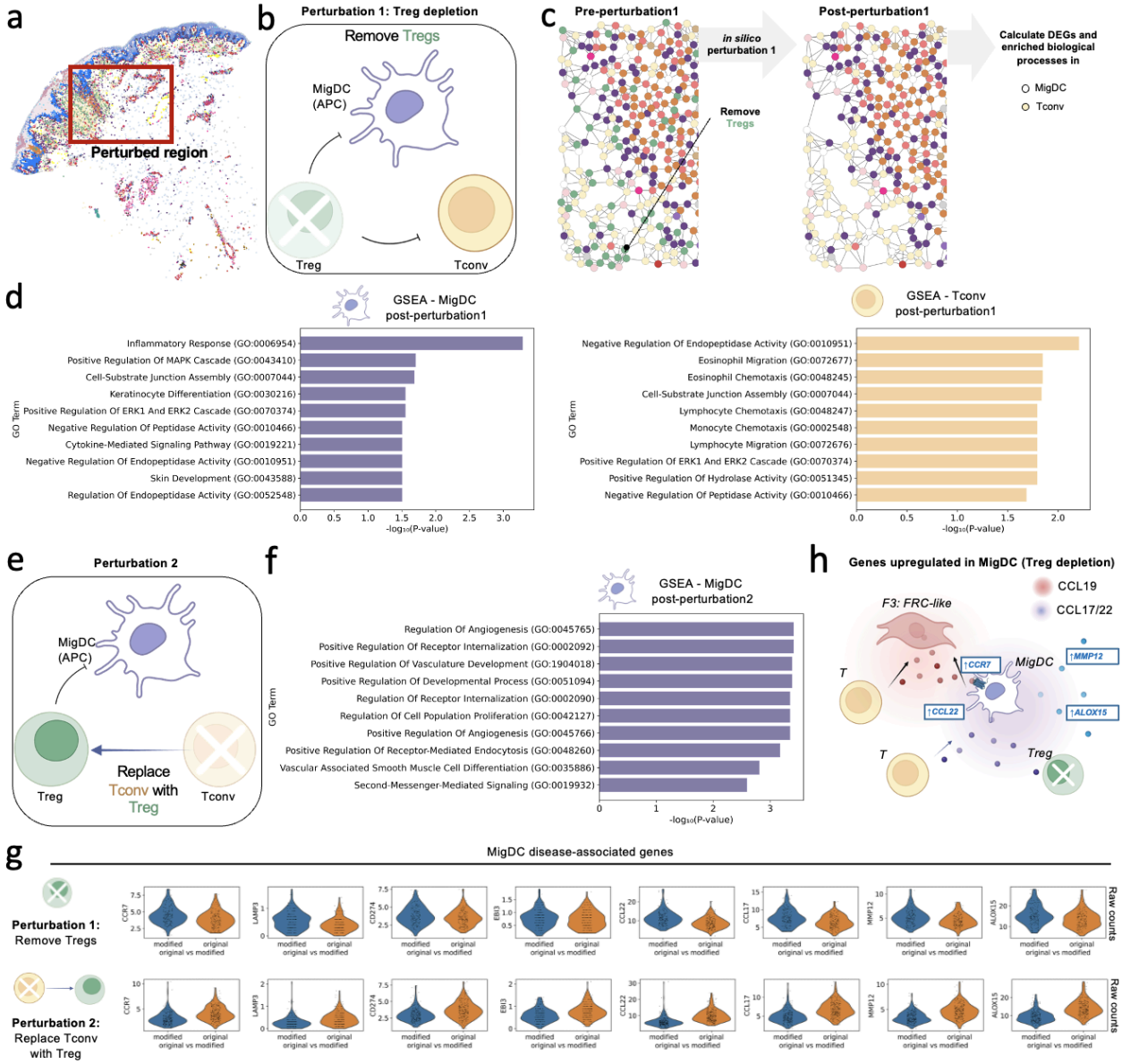

Fig. 3 | MintFlow *in silico* perturbation highlights therapeutic value of Tregs in atopic dermatitis. **a**, Region of tissue used for perturbation. **b**, Schematic representation of perturbation 1 (Treg depletion). **c**, Zoomed-in perturbation region to show changes before and after applying perturbation 1 (Treg depletion). **d**, Gene set enrichment analysis (GSEA) using Gene Ontology (GO) biological processes in MigDCs and T_{conv}s in perturbation 1. **e**, Schematic representation of perturbation 2 (Treg augmentation). **f**, Gene set enrichment analysis using (GO biological processes in MigDCs in perturbation 2. **g**, Violin plots of gene expression for migration and activation markers of MigDCs in perturbation 1 and 2. **h**, Schematic representation of perturbation 1 (Treg depletion), highlighting roles of upregulated genes in MigDC migration and recruitment of T cells.

MintFlow identifies inducible keloid-like stroma in cutaneous melanoma

Cell signalling is crucial in mediating interactions between cancer cells, immune cells, and the non-immune stroma in solid tumors[42]. To evaluate MintFlow's ability to identify microenvironment-induced factors in the TME, we applied it to a public human cutaneous melanoma dataset, profiled using 5000-plex Xenium[43] (Methods). After quality control, we identified 98 749 cells.

We identified the highest microenvironment scores outside of tumor nests (Fig. 4a,b). We identified 8 distinct microenvironment domains and their MGPs in melanoma, including two domains formed predominantly of tumor cells, which we termed *Melanoma1* and *Melanoma2* (Fig. 4c-e and Supplementary Fig. 6a). The cancer-predominant *Melanoma1* and *Melanoma2* domains occupied spatially-distinct regions in the skin, with *Melanoma2* forming a smaller, deeper nodule (Fig. 4f). While known melanoma marker genes (e.g. *MLANA*, *PRAME*) were present throughout both melanoma regions, the *Melanoma1* MGP uniquely contained genes that were not clearly evident in the *Melanoma2* domain (e.g. *EDNRB*, *CST1*, *BAALC*, *GDF15*) (Fig. 4e,g). Pathway analysis using these MGPs showed enrichment of biological processes of amino acid transport and glycogen catabolism for the *Melanoma1* domain, and cell migration and microtubule polymerization for *Melanoma2* (Supplementary Fig. 6b and Methods). This result suggested functionally distinct regions within the melanoma TME.

Immunotherapy is widely used in the treatment of advanced melanoma to promote anti-tumor T cell-mediated responses and can achieve sustained remission. Recent work has linked immunotherapy response to the state of cancer-associated fibroblasts (CAFs) in the stroma[44]. We therefore interrogated the *Stroma* microenvironment domain discriminated by MintFlow, which was formed predominantly of CAFs and T cells (Fig. 4d), to understand how this may influence T cell activity. The *Stroma* MGP included genes encoding *CXCL12* and extracellular matrix (ECM) proteins (Fig. 4e). *CXCL12* is a chemoattractant for cells expressing the receptor CXCR4, including T cells (Fig. 4h), and this inducible *CXCL12-CXCR4* axis has been reported to exclude T cells from tumor nests in human cancers[45,46]. Consistently, T cells in melanoma were largely located in the *Stroma* or *T_hub* domains (Fig. 4b,d), with the latter observed to

co-localize with stromal regions (Fig. 4i). *CXCL12* expression was high in these regions outside of tumor nests (Fig. 4e,j), suggesting that a stromal chemotactic axis segregates T cells away from tumor cells in melanoma, leading to a tumor-permissive environment.

ECM genes in the *Stroma* MGP included genes encoding collagens (*COL4A2*, *COL5A1*, *COL5A2, COL11A1*) and enzymes that cross-link collagen fibrils (*LOX*, *LOXL1*, *LOXL2*) (Fig. 4j and Supplementary Fig. 6c). T cells can be excluded from tumor nests by physical barriers including collagen fibres themselves[42]. Collagen cross-linking increases the stability of ECM fibres and is associated with worse outcomes in cancer[42]. To further investigate the nature of the stroma in melanoma, we scored the melanoma *Stroma* MGP across a dataset of skin fibroblasts from 23 different skin diseases profiled using scRNA-seq[25] (Methods). We found that the highest expression of the *Stroma* MGP was in cutaneous melanoma, confirming the relevance of the MGP across different technologies (Fig. 4k). Interestingly, we also observed high expression for the melanoma *Stroma* MGP in keloid scarring, which is a fibroproliferative scar with dense stroma that is characterized by increased cross-linking of collagen fibres[47]. Consistent with a microenvironment-induced scar-like stroma, the term “stromagenesis” has been used in cancer studies to describe bi-directional stromal signaling pathways that activate resident fibroblasts to a proliferative state[48], suggesting this inducible signaling network is captured by Mintflow.

In summary, our results suggest that active microenvironment signaling contributes to an inducible chemotactic and physical barrier against tumor cell infiltration in cutaneous melanoma, including an inducible keloid-like stroma.

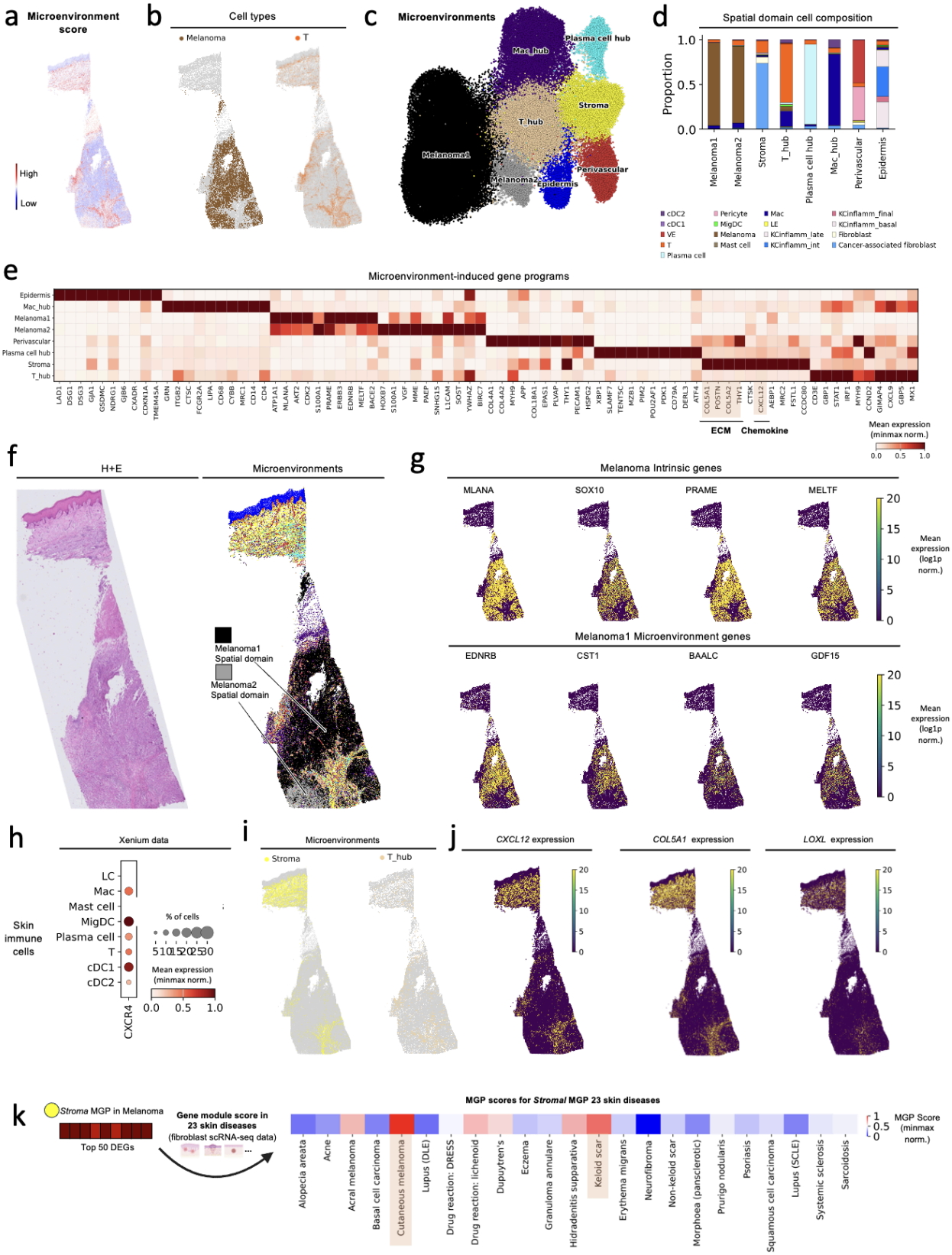
a
Microenvironment score
High
Low
b
Cell types
Melanoma
T
c
Microenvironments
Mac_hub
Plasma cell hub
Stroma
T_hub
Melanoma1
Melanoma2
Perivascular
Epidermis
d
Spatial domain cell composition
Proportion
1.0
0.5
0.0
Melanoma1
Melanoma2
Stroma
T_hub
Plasma cell hub
Mac_hub
Perivascular
Epidermis
cDC2
cDC1
VE
T
Plasma cell
Pericyte
MigDC
Melanoma
Mast cell
Mac
LE
KCinflamm_late
KCinflamm_int
KCinflamm_final
KCinflamm_basal
Fibroblast
Cancer-associated fibroblast
e
Microenvironment-induced gene programs
Epidermis
Mac_hub
Melanoma1
Melanoma2
Perivascular
Plasma cell hub
Stroma
T_hub
LAD1 DSG1 DSG3 GJA1 GSDMC NDRG1 GJB6 CXADR CDKN1A TMEM45A GRN ITGB2 CTSC FCGR2A LIPA CD68 CYBB MRC1 CD14 CD4 ATP1A1 MLANA AKT2 CDK2 S100A1 PRAME ERBB3 EDNRB MELTF BACE2 HOXB7 S100A1 VGF MME PAEP SNHG15 L1CAM SOST YWHAZ BIRC7 COL4A1 COL4A2 MYH9 APP COL18A1 EPAS1 PLVAP THY1 PECAM1 HSPG2 XBP1 SLAMF7 TENT5C MZB1 PIM2 POU2AF1 PDK1 CD79A DERL3 ATF4 COL5A1 POSTN COL5A2 THY1 CTSK CXCL12 AEBP1 MRC2 FSTL1 CCDC80 CD3E GBP1 STAT1 IRF1 MYH9 CCND2 GIMAP4 CXCL9 GBP5 MX1
ECM
Chemokine
Mean expression (minmax norm.)
0.0 0.5 1.0
f
H+E
Microenvironments
Melanoma1 Spatial domain
Melanoma2 Spatial domain
g
Melanoma Intrinsic genes
MLANA
SOX10
PRAME
MELTF
Mean expression (log1p norm.)
20
15
10
5
0
Melanoma1 Microenvironment genes
EDNRB
CST1
BAALC
GDF15
Mean expression (log1p norm.)
20
15
10
5
0
h
Xenium data
Skin immune cells
LC
Mac
Mast cell
MigDC
Plasma cell
T
cDC1
cDC2
CXCR4
% of cells
5 10 15 20 25 30
Mean expression (minmax norm.)
0.0 0.5 1.0
i
Microenvironments
Stroma
T_hub
j
CXCL12 expression
COL5A1 expression
LOXL expression
20
15
10
5
0
k
Stroma MGP in Melanoma
Top 50 DEGs
Gene module score in 23 skin diseases
(fibroblast scRNA-seq data)
MGP scores for Stromal MGP 23 skin diseases
Alopecia areata
Acne
Acral melanoma
Basal cell carcinoma
Cutaneous melanoma
Lupus (DLE)
Drug reaction: DRESS
Drug reaction: lichenoid
Dupuytren's
Eczema
Granuloma annulare
Hidradenitis supparativa
Keloid scar
Erythema migrans
Neurofibroma
Non-keloid scar
Morphoea (pansclerotic)
Prurigo nodularis
Psoriasis
Squamous cell carcinoma
Lupus (SCLE)
Systemic sclerosis
Sarcoidosis
1
0.5
0
MGP Score (minmax norm.)

Fig. 4 | Deciphering tumor microenvironment immune cell segregation in melanoma using MintFlow. **a**, Melanoma tissue section colored by microenvironment score. **b**, Tissue section colored by cell type (melanoma vs other and T cell vs other). **c**, UMAP visualization of the microenvironment-induced gene expression matrix for cutaneous melanoma, profiled using Xenium 5k. **d**, Cellular composition of microenvironment clusters. **e**, Microenvironment-induced gene programs (MGPs) for each microenvironment domain. **f**, Haematoxylin and eosin (H&E)-stained image of the tissue section from cutaneous melanoma and corresponding Xenium section colored by microenvironment domain. **g**, Differentially expressed genes for melanoma cells (intrinsic) (top row) and the Melanoma1 microenvironment domain (bottom row). **h**, Expression of CXCR4, the receptor for the CXCL12 ligand, by skin immune cells (Methods). **i**, Melanoma tissue section colored by microenvironment domains (Myofibrolast_T and T_hub). **j**, Melanoma tissue section colored by selected genes from the *Stroma* MGP. **k**, Gene module scores for the *Stroma* MGP across different skin diseases profiled using scRNA-seq data (Methods).

MintFlow identifies a tertiary lymphoid hotspot consisting of distinct T cell states in kidney cancer

To further evaluate the ability of MintFlow to resolve microenvironment-induced cell states within the TME, we applied it to spatial transcriptomic data from a patient with clear cell renal cell carcinoma (ccRCC), the most common form of adult kidney cancer. Three macroscopically distinct regions of the tumor core, as well as the tumor–normal interface where the cancer abuts non-neoplastic kidney tissue, were profiled using the 5000-plex Xenium platform (Fig. 5a; patient identifiers within Methods[49]). After integration and annotation, the dataset comprised 337,116 cells across 24 transcriptionally distinct cell types. MintFlow was applied to the integrated dataset to generate a latent space representing microenvironment-induced gene expression (Fig. 5b), achieving successful batch integration (Supplementary Fig. 7a) and robust alignment across cell types (Supplementary Fig. 7b). Spatial mapping of MintFlow-inferred microenvironment-induced cell states revealed regional variation in microenvironment score across the tissue (Fig. 5c). Within the tumor cores, discrete hotspots of elevated microenvironment score were observed, with a prominent structure within one tumor core (Fig. 5c; core 2).

Histopathological examination of this region revealed a dense lymphocytic aggregate (Fig. 5d), and MintFlow clustering indicated a predominance of T cells within the hotspot. Given its architecture and cellular composition, we hypothesized this structure represented a tertiary lymphoid structure (TLS), ectopic lymphoid aggregates known to arise in chronic inflammation and cancer, and previously associated with clinical outcome in ccRCC[50–52]. To validate this, we computed a TLS gene signature score based on expression of canonical TLS-associated genes (including CXCL13, LTA, and CXCR5)[53], confirming significant enrichment within the hotspot compared to surrounding tissue. To further dissect the immune architecture within the TLS, we subsetted MintFlow embeddings for T cells and performed unsupervised clustering. This

analysis revealed six distinct microenvironment-induced T cell states, three of which localized specifically within the TLS (Fig. 5e). These TLS-associated states, which we termed TLS Core 1, TLS Core 2, and TLS Border T cells, occupied spatially distinct domains within the aggregate (Fig. 5f). These microenvironment-induced states were not recoverable either by clustering MintFlow's intrinsic embeddings (Supplementary Fig. 8a) or by fine-grained reclustering of the original dataset (Supplementary Fig. 8b), highlighting MintFlow's unique ability to resolve spatially modulated T cell programs.

Differential gene expression analysis of the microenvironment-induced gene programs revealed distinct molecular signatures (Fig. 5g). Consistent with previous observations in ccRCC[54,55], tumor-infiltrating T cells exhibited enrichment for exhaustion markers such as *HAVCR2, TOX, LAG3*, and were expressed at the highest level by T cells within the TLS border zone. Tumor-infiltrating T cells also enriched for *CXCR3*, with its cognate ligands, *CXCL9* and *CXCL10*, spatially enriched within the TLS (Supplementary Fig. 9). MintFlow identified similar TLS-associated T cell states across Xenium data of additional ccRCC patients, with MGPs mapping to lymphoid aggregates observed on histology (Supplementary Fig. 10). These findings demonstrate MintFlow's ability to uncover microenvironment-induced immune architecture not readily detectable by conventional analyses, highlighting T cell states that are enriched within the TLS in ccRCC.

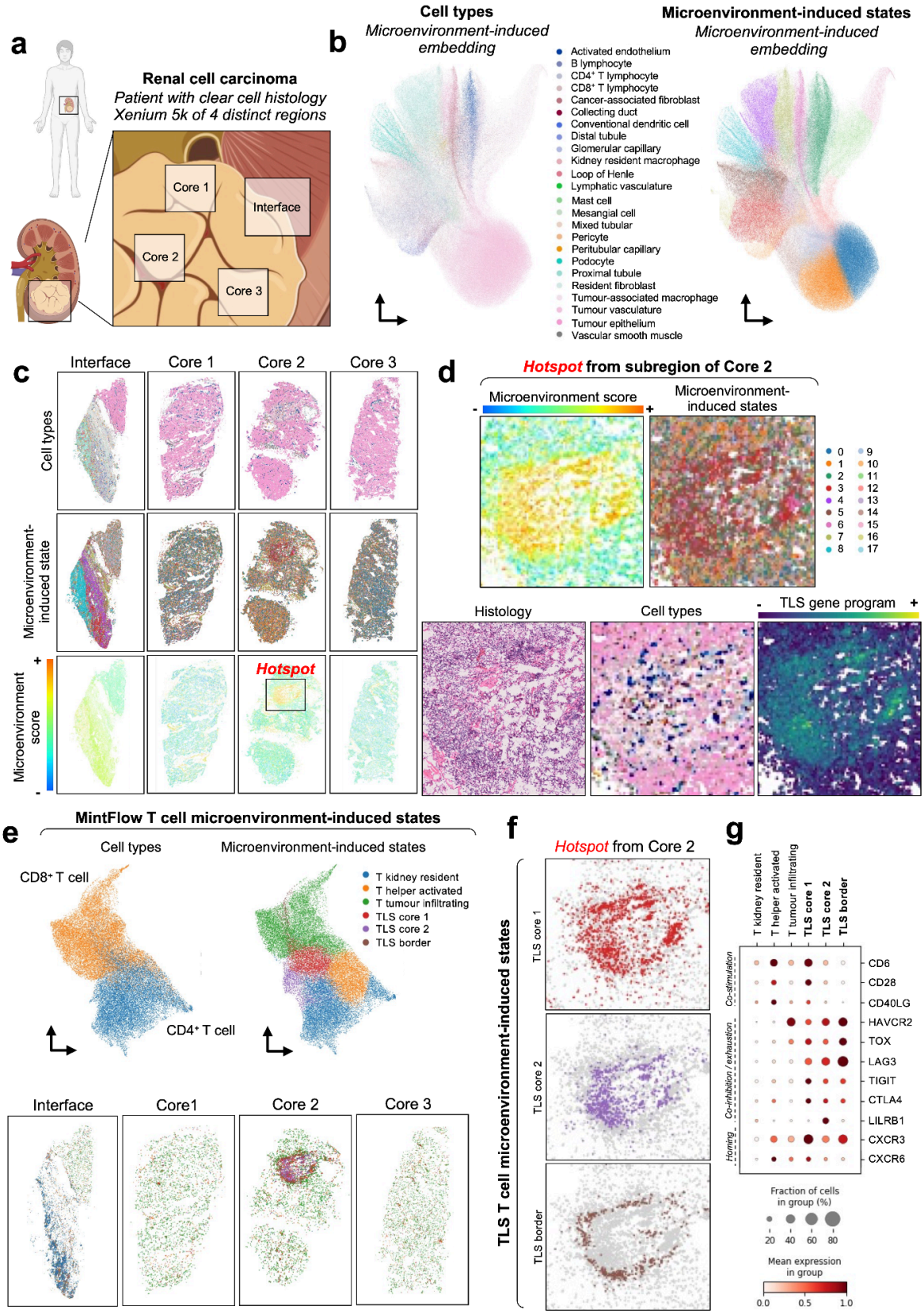
a
Renal cell carcinoma
Patient with clear cell histology
Xenium 5k of 4 distinct regions
Core 1
Interface
Core 2
Core 3
b
Cell types
Microenvironment-induced embedding
Activated endothelium
B lymphocyte
CD4⁺ T lymphocyte
CD8⁺ T lymphocyte
Cancer-associated fibroblast
Collecting duct
Conventional dendritic cell
Distal tubule
Glomerular capillary
Kidney resident macrophage
Loop of Henle
Lymphatic vasculature
Mast cell
Mesangial cell
Mixed tubular
Pericyte
Peritubular capillary
Podocyte
Proximal tubule
Resident fibroblast
Tumour-associated macrophage
Tumour vasculature
Tumour epithelium
Vascular smooth muscle
Microenvironment-induced states
Microenvironment-induced embedding
c
Interface
Core 1
Core 2
Core 3
Cell types
Microenvironment-induced state
Microenvironment score
Hotspot
d
Hotspot from subregion of Core 2
Microenvironment score
Microenvironment-induced states
Histology
Cell types
TLS gene program
e
MintFlow T cell microenvironment-induced states
Cell types
Microenvironment-induced states
CD8⁺ T cell
CD4⁺ T cell
T kidney resident
T helper activated
T tumour infiltrating
TLS core 1
TLS core 2
TLS border
Interface
Core1
Core 2
Core 3
f
Hotspot from Core 2
TLS T cell microenvironment-induced states
TLS core 1
TLS core 2
TLS border
g
T kidney resident
T helper activated
T tumour infiltrating
TLS core 1
TLS core 2
TLS border
Co-stimulation
Co-inhibition / exhaustion
Homing
CD6
CD28
CD40LG
HAVCR2
TOX
LAG3
TIGIT
CTLA4
LILRB1
CXCR3
CXCR6
Fraction of cells in group (%)
20 40 60 80
Mean expression in group
0.0 0.5 1.0

Fig. 5 | MintFlow analysis of microenvironment-induced cell states in kidney cancer. a, Schematic illustrating the spatial transcriptomic profiling strategy in a nephrectomy specimen from a patient with clear cell renal cell carcinoma (ccRCC). Four anatomically distinct tumor subregions were sampled: Core 1, Core 2, Core 3, and the tumor–normal interface **b**, UMAP visualizations of MintFlow-inferred microenvironment-induced gene expression profiles, colored by cell type (left) and MintFlow clusters (right). **c**, Spatial mapping of each subregion showing cell types (top row), MintFlow microenvironment-induced clusters (middle row), and computed microenvironment score (bottom row). A signaling hotspot is highlighted in Core 2. **d**, High-resolution profiling of the hotspot region displaying microenvironment score, MintFlow clusters, histological image, annotated cell types, and a tertiary lymphoid structure (TLS) module score. The TLS score was calculated using the following genes: CXCL13, CCR7, LTA, CXCR5, CD8A, CD4, CCL19, CD79A, MS4A1, and CD3E. **e**, Subclustering of T cells using MintFlow: UMAPs showing original cell type annotations (left) and MintFlow-derived microenvironment-induced T cell states (right), alongside spatial distribution of these states across the four tissue subregions (below). **f**, Magnified view of the TLS region showing spatial localization of MintFlow-inferred T cell states: TLS Core 1, TLS Core 2, and TLS Border T cells. **g**, Dot plot of differentially expressed genes across MintFlow-inferred TLS T cell states. Markers of immune inhibition and exhaustion (e.g., HAVCR2, LAG3) are enriched in tumor-infiltrating and TLS-resident T cells, while CXCR3 ligands (CXCL10, CXCL11) are specifically enriched in TLS Border T cells.

Using MintFlow to reveal, prioritize and predict reprogramming of inhibitory macrophage-T cell crosstalk within the TLS of kidney cancer

Having identified distinct microenvironment-induced T cell states within the TLS, we next sought to determine whether these populations could be retrospectively identified in single-cell RNA sequencing (scRNA-seq) data lacking spatial information. We reanalyzed a published scRNA-seq dataset of ccRCC[49], comprising 147,917 tumor-infiltrating cells from 10 patients, including the donor from whom the Xenium spatial transcriptomics data were derived (Fig. 6a). Using MintFlow-derived gene programs for the TLS Core 1, TLS Core 2, and TLS Border T cells, we projected these signatures onto the T cell compartment of the scRNA-seq dataset (Fig. 6b). Expression of the aggregated TLS T cell gene program was distributed across T cell subclusters without clear demarcation, highlighting the difficulty of identifying spatially organized immune states without explicit spatial resolution. Importantly, the TLS T cell programs were detectable across patients spanning low, intermediate and high Leibovich risk groups (Fig. 6b), supporting the generalizability of these states across clinical stages.

Given the immunosuppressed phenotype observed in TLS T cells, we hypothesized that specific cell–cell interactions within the TLS niche may drive their dysfunctional state. To explore this, we performed ligand–receptor interaction analysis across the scRNA-seq data, treating TLS T cells as a discrete population. Among all cell types in the ccRCC microenvironment, TLS T cells exhibited the highest predicted number of interactions with

myeloid populations, particularly macrophages (Fig. 6c). Examination of the top 100 ligand–receptor pairs revealed enrichment for major histocompatibility complex (MHC) class I and II interactions, as well as co-inhibitory signals, including molecules such as *LAG3*, *HAVCR2*, and others known to mediate T cell exhaustion (Supplementary Fig. 11). We next returned to the spatial Xenium dataset to validate the presence and spatial localization of macrophages potentially responsible for inhibitory signaling within the TLS. Subclustering MintFlow's macrophage latent space for microenvironment-induced gene expression resolved a distinct tumor-associated macrophage subset localized specifically to the TLS (Fig. 6d), characterized by high expression of *TREM2* and *CCR1*. Differential expression analysis of this TLS-associated macrophage subset revealed enrichment for pathways linked to antigen presentation, interferon response, and T cell co-inhibition, consistent with the predicted ligand–receptor interactions. Analysis of other stromal populations, including vasculature (Supplementary Fig. 12a) and fibroblasts (Supplementary Fig. 12b), revealed no distinct microenvironment-induced cell states specifically localized to the TLS, suggesting that macrophage-T cell interactions are the primary mediators of immune suppression within this microenvironment domain.

We next leveraged the generative modeling capabilities of MintFlow to perform *in silico* perturbation of macrophage-T cell interactions within the TLS of ccRCC. Specifically, we performed a perturbation in which the TLS-associated macrophage subset identified above was deleted, predicting how T cell gene expression states would respond in the absence of suppressive myeloid signals (Fig. 6e). DEG analysis following macrophage deletion revealed consistent reprogramming across each microenvironment-induced TLS T cell state. Molecules associated with T cell co-inhibition and exhaustion, including *PD-L2, TIM3, VSIR, CD276, LILRB1* and *LAIR1*, were downregulated, whereas reprogrammed T cells exhibited increased expression of markers indicating TCR signalling (PLCG1, STIM1, TRAF6) and interleukin receptors (IL4R, IL6ST, IL15RA). These findings suggest that local disruption of macrophage-mediated signals within the TLS restores an activated T cell phenotype *in silico*.

To assess the clinical significance of MintFlow-predicted reprogramming, we applied the microenvironment-induced gene programs to bulk RNA sequencing data from 606 ccRCC tumors in The Cancer Genome Atlas (TCGA) cohort. For each TLS T cell state, we computed gene expression scores across patients and stratified individuals into 'high' and 'low' expression groups. Kaplan–Meier survival analysis using available overall survival data revealed that neither the TLS Core 1, TLS Core 2 nor TLS macrophage gene programs were significantly associated with patient outcome (Supplementary Fig. 13). However, high expression of the TLS Border T cell program, representing the peripheral, suppressive T cell state within the TLS, was significantly associated with worse overall survival ($p = 0.0073$) (Fig. 6f). When we applied the MintFlow-inferred gene program for TLS Border T cells after macrophage removal *in silico*, high expression of the reprogrammed state was associated with a survival advantage ($p = 0.0034$). These findings suggest that targeted modulation of macrophage–T cell interactions within

tertiary lymphoid structures could therapeutically reprogram local immunity and potentially improve patient outcomes in ccRCC.

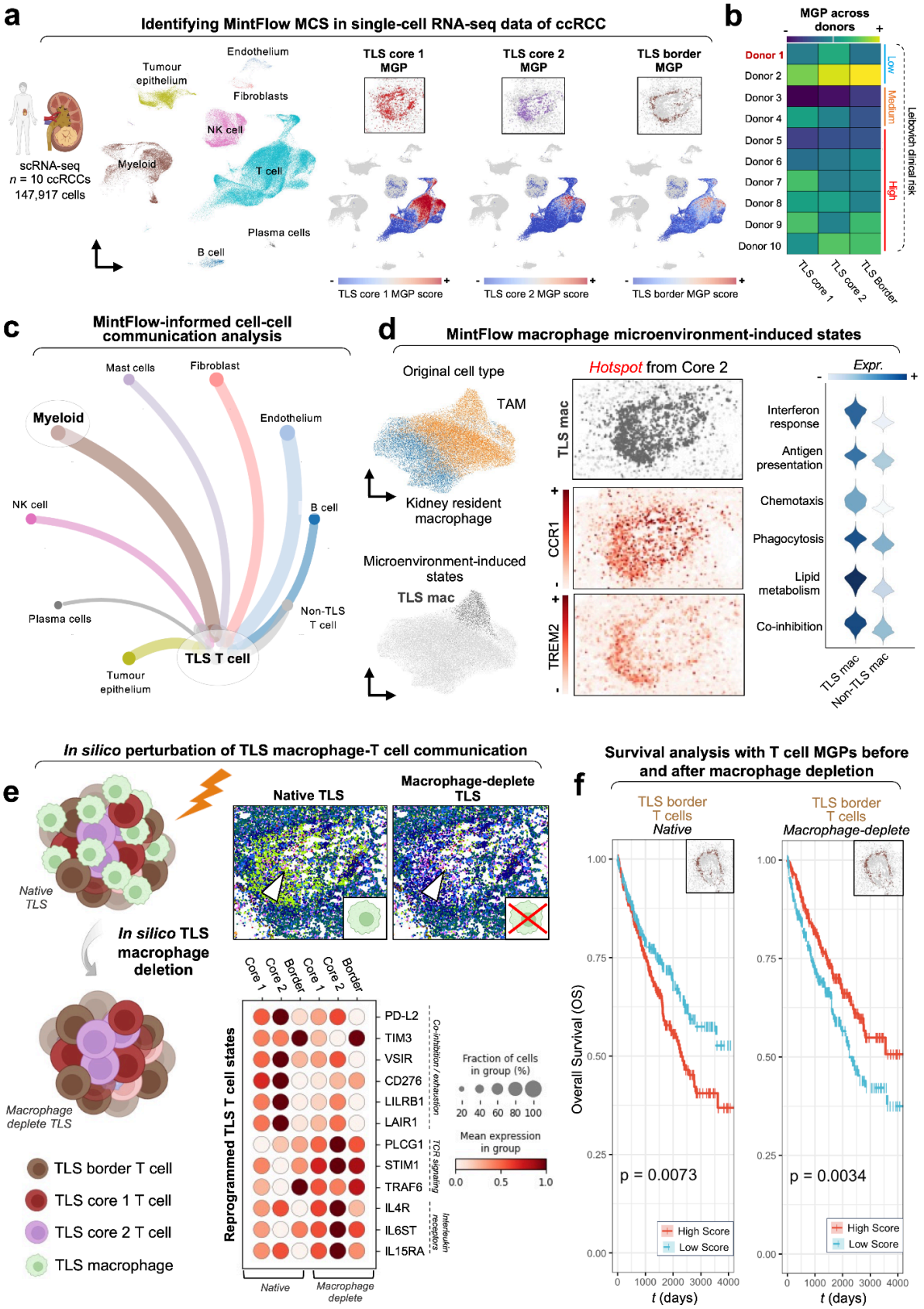
a
Identifying MintFlow MCS in single-cell RNA-seq data of ccRCC
scRNA-seq
n = 10 ccRCCs
147,917 cells
Tumour epithelium
Endothelium
Fibroblasts
NK cell
Myeloid
T cell
Plasma cells
B cell
TLS core 1 MGP
TLS core 2 MGP
TLS border MGP
TLS core 1 MGP score
TLS core 2 MGP score
TLS border MGP score
b
MGP across donors
Donor 1
Donor 2
Donor 3
Donor 4
Donor 5
Donor 6
Donor 7
Donor 8
Donor 9
Donor 10
Low
Medium
High
Leibovitch clinical risk
TLS core 1
TLS core 2
TLS Border
c
MintFlow-informed cell-cell communication analysis
Mast cells
Fibroblast
Myeloid
Endothelium
NK cell
B cell
Plasma cells
Non-TLS T cell
TLS T cell
Tumour epithelium
d
MintFlow macrophage microenvironment-induced states
Original cell type
TAM
Kidney resident macrophage
Microenvironment-induced states
TLS mac
Hotspot from Core 2
TLS mac
CCR1
TREM2
Expr.
Interferon response
Antigen presentation
Chemotaxis
Phagocytosis
Lipid metabolism
Co-inhibition
TLS mac
Non-TLS mac
In silico perturbation of TLS macrophage-T cell communication
e
Native TLS
In silico TLS macrophage deletion
Macrophage deplete TLS
Native TLS
Macrophage-deplete TLS
TLS border T cell
TLS core 1 T cell
TLS core 2 T cell
TLS macrophage
Core 1
Core 2
Border
Core 1
Core 2
Border
Reprogrammed TLS T cell states
PD-L2
TIM3
VSIR
CD276
LILRB1
LAIR1
PLCG1
STIM1
TRAF6
IL4R
IL6ST
IL15RA
Co-inhibition / exhaustion
TCR signaling
Interleukin receptors
Fraction of cells in group (%)
20 40 60 80 100
Mean expression in group
0.0 0.5 1.0
Native
Macrophage deplete
Survival analysis with T cell MGPs before and after macrophage depletion
f
TLS border T cells Native
TLS border T cells Macrophage-deplete
Overall Survival (OS)
p = 0.0073
p = 0.0034
High Score
Low Score
t (days)

Fig. 6 | Application of MintFlow to uncover cell–cell communication, perform in silico perturbation, and stratify patient survival in kidney cancer. a, Left: UMAP visualization of single-cell RNA sequencing (scRNA-seq) data from 10 patients with clear cell renal cell carcinoma (ccRCC), including one patient whose tumor was also profiled by spatial transcriptomics in this study. Cells are colored by broad cell type annotation. Right: Feature plots showing recovery of the MintFlow-derived TLS T cell microenvironment-induced gene programs within the scRNA-seq dataset. **b**, Heatmap displaying TLS T cell program scores across T cells from each patient in the scRNA-seq cohort, grouped by Leibovich grade: a clinical risk classification for ccRCC. **c**, Ligand–receptor interaction analysis using LIANA applied to the scRNA-seq data. TLS T cells were identified based on MintFlow program scores. The circle plot illustrates predicted interaction strength between TLS and non-TLS T cells and other major cell types. **d**, Subclustering of macrophages using MintFlow microenvironment-induced embeddings from the Xenium dataset. UMAPs show original macrophage annotations (top) and MintFlow-defined TLS macrophages (bottom). Spatial localization of TLS macrophages is shown alongside expression of key markers *TREM2* (middle) and *CCR1* (bottom). Violin plot indicates enrichment of immune regulatory pathways—antigen presentation, interferon response, and T cell co-inhibition, within TLS macrophages compared to all other macrophages. **e**, *In silico* perturbation analysis of TLS macrophages using MintFlow. Schematic (left) and spatial visualization (top right) illustrate macrophage removal. Dot plot (bottom right) shows top differentially expressed genes in TLS T cells before and after perturbation. Removal of macrophages led to decreased expression of T cell co-inhibition and exhaustion markers (PD-L2, TIM3, VSIR, CD276, LILRB1, LAIR1) and increased expression of markers of TCR signalling (PLCG1, STIM1, TRAF6) and interleukin receptors (IL4R, IL6ST, IL15RA). **f**, Kaplan–Meier survival analysis using TCGA bulk RNA-seq data from 606 ccRCC patients. Patients were stratified based on expression of the TLS Border T cell program before (left) and after (right) in silico macrophage removal. High expression of the original TLS Border T cell program was associated with worse survival ($p = 0.0073$), while the perturbed gene program predicted a survival advantage ($p = 0.0034$).

Discussion

Spatial transcriptomics offers unprecedented insight into tissue organization and how it is altered in disease. However, current computational approaches remain largely descriptive and do not resolve how the microenvironment actively shapes cellular gene expression, limiting their utility for mechanistic discovery, patient stratification, or therapeutic prediction. Here, we introduce MintFlow, a deep generative AI model that learns how spatial context reprograms cell states. MintFlow identifies microenvironment-induced cell states and gene programs that underpin human pathology. Importantly, MintFlow supports *in silico* perturbation, enabling users to simulate how removal or replacement of specific cell types reconfigures local transcriptional states. Across multiple diseases, MintFlow not only recapitulates established

spatial features but also uncovers previously unrecognized, clinically relevant cell states and programs dictated by the microenvironment in inflammatory and malignant diseased contexts. These findings demonstrate MintFlow's potential as a predictive framework for spatial biology, with broad applications for virtual tissue reprogramming to guide biomarker discovery and drug repurposing.

A central strength of MintFlow lies in its ability to recover microenvironment-induced transcriptional programs that are often obscured in traditional analyses. Applied across three distinct diseases, MintFlow uncovered both disease-specific and generalizable spatial cell states. In atopic dermatitis, it identified a T cell–dendritic cell activation hub for type 2 immunity, conserved across other type 2–inflammatory diseases such as eosinophilic chronic rhinosinusitis CRSwNP. Mintflow also identified superficial *CD8+IL13+ITGAE+* resident memory–like T cells as a microenvironment-induced state, consistent with recent murine findings[34]. While resident memory T cells have been well described in psoriasis and vitiligo[56,57], they are not well recognized in atopic dermatitis[32]. Conversely, in melanoma, MintFlow resolved a fibroblast-rich, collagen-crosslinked stromal program expressing *CXCL12*, associated with T cell exclusion and resembling fibrotic keloid tissue. Finally, in ccRCC, MintFlow prioritized TLS as a hotspot of signaling activity, composed of three spatially distinct T cell states. This included an immunosuppressed border population not detectable by conventional clustering, described by a gene program associated with poor survival in a large and heterogeneous cohort of patients.

A defining feature of MintFlow is its capacity for *in silico* perturbation of the tissue, leveraging generative AI to predict how modifying the microenvironment alters gene expression. In atopic dermatitis, MintFlow simulated the depletion or augmentation of Treg cells, recapitulating known biology: Treg depletion amplified inflammatory signaling, consistent with FOXP3-mutant IPEX syndrome, while Treg augmentation suppressed inflammatory pathways and modulated vascular signaling, supporting therapeutic strategies using adoptive Treg therapy[38]. In ccRCC, MintFlow identified macrophage–T cell interactions within TLS as key mediators of local immune suppression. Simulated deletion of TLS-associated macrophages lead to downregulation of co-inhibition and exhaustion markers in TLS T cells, and instead, reprogrammed them toward more activated states. When *in silico* reprogrammed T cell states were projected onto TCGA ccRCC bulk tumor profiles, they became associated with a survival advantage, demonstrating that MintFlow goes beyond spatially resolving cell–cell interactions but also links these to clinically meaningful outcomes. These findings position MintFlow as a powerful framework for uncovering spatial drivers of cellular dysfunction and simulating therapeutic rewiring of diseased tissue microenvironments. Many of the perturbations explored by MintFlow, such as cell type-specific depletion within intact tissue architecture, are challenging or unfeasible to perform at scale using *in vitro* models or animal systems, highlighting the unique value of virtual experimentation in guiding mechanistic and translational hypotheses. Of known candidates identified by MintFlow, several have already shown utility in translational settings. For example, of the TLS T cell genes downregulated by *in silico*

macrophage deletion in ccRCC, LAIR1 is upregulated in RCC and its expression correlates with poor survival[58], TIM3 expression is associated with response to immunotherapy[59] and LILRB1 inhibitors are undergoing early phase clinical trials in kidney cancer patients[60]. We also tested the sensitivity of MintFlow tissue perturbations to the number of cells altered in the tissue and measured the effect size change in response to the perturbations. We observed that as a larger subpopulation of target cells are perturbed, the expression of the considered genes also changed incrementally (Supplementary Fig. 19). Although this effect is noticeable for both depletion and augmentation AD perturbations, the latter has a more significant incremental effect (Supplementary Fig. 19a) since it has a direct and deterministic effect on the MCC of a subpopulation of cells in tissue. However, in the depletion perturbation the neighborhood graph is recreated and, as a result, the discarded cell type may still appear in the MCC of a cell due to, e.g., cells of that type appearing as new neighbors in the newly created neighborhood graph.

Although MintFlow introduces a novel approach for modeling microenvironment-induced cell variation and simulating *in silico* perturbations, several limitations remain. One includes sensitivity to low read counts (Supplementary Fig. 2 and 3) and the need for consistent gene panels across tissue sections. While the flow matching process is computationally intensive during training, our implementation incorporates a neighbor sampling strategy to enhance scalability, enabling training the model on multiple tissue sections encompassing millions of cells (Methods). Future work could expand the modeling framework beyond multiple tissue sections to support training on multi-tissue spatial atlases, enabling transfer learning across datasets and analysis of microenvironmental influences at atlas scale. Additionally, while we have released MintFlow as an open source Python package, training MintFlow can be challenging and requires dataset-specific fine-tuning of hyperparameters due to its complex modeling architecture. To support adoption, we provide detailed documentation and guidance at https://mintflow.readthedocs.io.

We envision MintFlow as a transformative tool for spatial transcriptomics analysis in both basic research and clinical applications. Its ability to disentangle spatial drivers of gene expression, simulate cellular perturbations, and predict outcomes, positions it as a platform for therapeutic hypothesis generation, drug response modeling and patient stratification. By integrating MintFlow into spatial workflows, researchers and clinicians can gain mechanistic insight into disease architecture and virtually test interventions. This framework has the potential to revolutionize how we analyze tissue microenvironments, accelerating the discovery of novel biomarkers and therapies to ultimately improve the translation of biological discovery to patient outcomes.

Data Availability

Public Xenium FFPE skin sections were downloaded from 10x Genomics (https://www.10xgenomics.com/datasets/xenium-prime-ffpe-human-skin). Simulated data is

available for download as described at https://github.com/Lotfollahi-lab/mintflow-reproducibility. All other data will be made available soon.

Code Availability

MintFlow is available as a Python package, maintained at https://github.com/Lotfollahi-lab/mintflow. All code to reproduce experiments, including benchmarking and analyses, is available at https://github.com/Lotfollahi-lab/mintflow-reproducibility. We provide comprehensive documentation encompassing tutorials and a user guide at https://mintflow.readthedocs.io/.

Acknowledgments

S.B. is supported by the Helmholtz Association under the joint research school "Munich School for Data Science—MUDS". D.J.J. is supported by a Wellcome Trust Accelerator Award (314710/Z/24/Z), the Foulkes Foundation and the Specialised Foundation Programme at the East of England NHS Deanery. L.S. is supported by a Wellcome Clinical Research Training Fellowship and Trinity Internal Graduate Studentship. S.B. is grateful to Paula, Pebble and Pixel Villa Fulton for their inspirational support.

Author Contributions

M.L. and M.H. conceived the project and designed the experiments. A.A. designed and implemented the model with contributions from S.B., A.M. and theoretical feedback and contributions from S.V. L.S., D.J.J., M.R.S., K.R. and M.R.C. performed data analysis. A.B., B.R., C.T., M. Patel, M. Prete, S. Makarchuk, S. Mahil, T.L., H.S., A.R.F., K. Roberts, A.L.T., and C.S. contributed to sample collection, performing experiments, data generation and processing. C.E.V. and G.T. supported M.R.S. T.M. supported D.J.J., contributed to data generation and provided kidney samples. O.A.B., M.H. and M.L. supervised the work. S.B., A.A., D.J.J., M.R.S., O.A.B., M.H., M.L. and L.S. wrote the paper.

Competing Interests

M.L. owns interests in Relation Therapeutics and is a scientific cofounder and part-time employee at AIVIVO.

Methods

Model overview and assumptions

Our proposed generative model (Supplementary Fig. 14) explicitly models intrinsic as well as spatial signals between a cell and its microenvironment, generating intrinsic and microenvironment-induced embeddings for each cell. A cell's intrinsic embedding is conditioned on its cell type label, while its microenvironment-induced embedding is conditioned on its microenvironment cell type composition (MCC). To define cells' microenvironments, a k-Nearest Neighbors graph (k=5) is created where nodes represent cells and edges connect neighboring cells. A cell's set of neighbors in the graph is considered its microenvironment, and its MCC is computed as the proportion of each cell type within its microenvironment. Cells' embeddings and their relation are defined as follows. The variable s_n^{out}, a priori conditioned on cell type, is the signal that the n-th cell communicates to neighboring cells in the microenvironment. In the n-the cell, the s_m^{out} signals from all neighbor cells m in the microenvironment are received and aggregated in s_n^{in} via simple neighborhood averaging: $s_n^{in} = \frac{\sum_{m \in Neigh(n)} s_m^{out}}{|Neigh(n)|}$, where $Neigh(n)$ is the set of neighbors of the n-th cell, and $|Neigh(n)|$ is its node degree. As s_m^{out} is a priori conditioned on the cell type of cell m, the aggregation indirectly conditions s_n^{in} on the microenvironment cell type composition of cell n. Intuitively, s_n^{out} is expected to contain information about the signal that the n-th cell secrets into its microenvironment, while s_n^{in} contains information about the signal that the n-th cell receives from its microenvironment. The variable z_n, apriori conditioned on cell type, captures the intrinsic variation of the n-th cell, which is not influenced by its microenvironment. Intuitively, z_n comprises internal signals such as the expression of receptors, cell cycle regulators, and housekeeping genes. We assume the expression in each cell has two components:

1. The part which is not triggered by a signal from outside: In the n-th cell this part of expression is encoded in x_n^{int}. It is only affected by the internal cell state z_n (Supplementary Fig. 14).

2. The part which is triggered by a signal from outside: In the n-th cell this part of expression is encoded in x_n^{mic}. It is affected by the signal that the n-th cell receives from its neighbors, encoded in variable s_n^{in}, and internal properties that are relevant for processing these external signals such as the receptor expression which is encoded in the variable z_n (Supplementary Fig. 14).

Since training flow-based generative models on high-dimensional data is impractical[61], we perform flow matching in latent space, using a neural ordinary differential equation (neural ODE)[62] decoder to obtain $\bar{x}_n^{int}$ and $\bar{x}_n^{mic}$, which are lower-dimensional representations of the intrinsic (x_n^{int}) and microenvironment-induced (x_n^{mic}) components of expression. We then employ decoders that take in $\bar{x}_n^{int}$ and $\bar{x}_n^{mic}$ and generate the intrinsic and microenvironment-induced gene expression vectors x_n^{int} and x_n^{mic}, respectively. We denote the count readout in the n-th cell by x_n. We have that $x_n = x_n^{int} + x_n^{mic}$, where $x_n, x_n^{int}, x_n^{mic} \in R^{|genes|}$ and $|genes|$ is the number of genes. The readouts x_n are observed while the vectors x_n^{int} and x_n^{mic} are latent. Note that we could have directly decoded x_n from $\bar{x}_n^{int}$ and $\bar{x}_n^{mic}$, completely bypassing and discarding x_n^{int} and x_n^{mic}. However, the inclusion of x_n^{int} and x_n^{mic} provides an explicit decomposition of the readout matrix as $X = X^{int} + X^{mic}$, where X^{int} and X^{mic} are cell by gene matrices and can directly be used for biological analysis. In other words, this design choice adds interpretability to our model thereby removing the need for archetypal or linear probe analysis on the low-dimensional embeddings, which is used by other methods[10].

Notes on identifiability and objective terms

Our proposed model is a deep generative model to generate expression data $\{x_n\}_{n=1}^{N}$. Such a model with non-linear decoders is known to be unidentifiable in general[63]. However, a line of research guarantees identifiability if latent factors are conditioned on some side information[64–67]. Inspired by this, we condition the latent embeddings z_n and s_n^{out} of the n-th cell on its cell type annotation, denoted by the one-hot encoded vector t_n (Supplementary Fig. 14). In particular, for s_n^{out} we define a conditional normal distribution whose mean is a "linear" function of t_n as follows:

$$p\left(s_n^{out} | t_n\right) = N\left(s_n^{out}\,;\, \mu_u^T t_n,\ exp(\sigma\left(t_n\right)\right). \tag{1}$$

Therefore, for the n-th cell according to Eq. (1) the prior on s_n^{in} is a normal distribution with mean $\frac{\mu_u^T}{|Neigh(n)|} \sum_{m \in Neigh(n)} t_m$. Note that since t_m are one-hot encoded vectors, the term $\frac{1}{|Neigh(n)|} \sum_{m \in Neigh(n)} t_m$ contains the frequency of different cell types among neighbors of the n-th cell. We refer to this vector as MCC (microenvironment cell type composition) and to the cell type one-hot encoded vector as CT (cell type).

With this setup, we mimic the iVAE method[64] that guarantees identifiability by conditioning the latent embedding on some label u (Supplementary Fig. 15a). In our case, we condition z and s^{in} on CT and MCC (Supplementary Fig. 15b). The only iVAE[64] assumption that we violate at this point is that in our case the gene expression vectors x could be interleaved and dependent among neighboring cells while in iVAE[64] the x vectors are assumed independent.

Consequently, in our proposed method the vector $\left[z, s^{in}\right]$ is expected to be identifiable up to permutation of its dimensions. Notably the $dim(z) + dim(s)$ dimensions of the vector $\left[z, s^{in}\right]$ can freely permute, hindering the separation of intrinsic and microenvironment-induced embeddings. To identify z and s^{in}, we therefore introduce two additional objectives:

$Objective_1$: $CT\ being\ predictable\ from\ z\ of\ a\ cell.$

$Objective_2$: $MCC\ being\ predictable\ from\ s^{in}\ of\ a\ cell.$

Intuitively, among the $dim(z) + dim(s)$ dimensions of the vector $\left[z, s^{in}\right]$, $dim(z)$ (resp. $dim(s)$) dimensions that are related to CT (resp. MCC) are assigned to z (resp. s^{in}). Importantly, although $Ojbective_1$ and $Objective_2$ encourage the identification of z and s^{in}, the dimensions of those vectors can still freely and benignly permute. In a cell type homogeneous region the CT and MCC vectors become equal, impairing their ability to identify the intrinsic/microenvironment-induced parts of the vector $\left[z, s^{in}\right]$. However, the existence of non-homogenous regions in other tissue regions make the intrinsic/microenvironment-induced dimensions identifiable.

Let $F(.,.)$ be the decoder for the observed gene expression vectors, i.e. $F\left(z, s^{in}\right) = x$. For the sake of argument, let us also assume that no dimensionality reduction happens, i.e. the variables $\bar{x}_n^{int}$ and $\bar{x}_n^{mic}$ would be omitted (Supplementary Fig. 15c). Although so far we discussed why the vectors z and s^{in} are expected to be identifiable up to permutation, this doesn't fulfil the objective of the proposed method, because recall that besides identifying the function $F(.,.)$, our goal is to decompose the gene expression vector x to x^{int} and x^{mic}. Let's assume that the function $F(.,.)$ is known and we want to decompose it as

$$F\left(z, s^{in}\right) = G\left(z, s^{in}\right) + H(z)\ where\quad G\left(z, s^{in}\right) = x^{mic},\quad H(z) = x^{int},\quad F\left(z, s^{in}\right) = x. \tag{2}$$

One unsatisfactory solution to the decomposition of Eq. 2 is $H(z)$ being zero for all z, and $F(.,.) = G(.,.)$ for all z and s^{in}. In other words, this unsatisfactory solution effectively ignores the path $z \rightarrow \bar{x}^{int} \rightarrow x^{int}$ (Supplementary Fig. 14a) and, for all cells, puts all read counts x in x^{mic}. Conversely, the decoder $G\left(z, s^{in}\right)$ may ignore s^{in} by putting all the dataset variation in z, leading

to another unsatisfactory solution. Empirically, we found the former bad solution quite likely to be found by the method. To avoid these cases we introduce two additional objectives:

$Objective_3$: $CT\ being\ predictable\ from\ \bar{x}^{int}\ of\ a\ cell.$

$Objective_4$: $MCC\ being\ predictable\ from\ \bar{x}^{mic}\ of\ a\ cell.$

Putting aside unwanted solutions, without any additional assumptions the decomposition of Eq. 2 is not unique. Because for any arbitrary $H(z)$, $G\left(z, s^{in}\right)$ could be simply defined as $F\left(z, s^{in}\right) - H(z)$ and Eq. 2 holds. To make the decomposition of Eq. 2 unique, we impose conditions related to optimal transport.

Proposition 1. Consider the decomposition of Eq. 2 where $F(.,.)$ is known and $G(.,.)$ and $H(.)$ are to be found. Let λ be an arbitrary positive scalar and $c(.,.)$ be the Euclidean distance. If $G(.,.)$ and $H(.)$ are constrained to optimize the cost functional of Eq. 3, then in the decomposition of Eq. 2 $G(.,.)$ and $H(.)$ are unique. Put differently, the optimization functional problem of Eq. 3 - when $H(.)$ and $G(.,.)$ are constrained to sum up to a known function $F(.,.)$ according to Eq. 2 - has a unique solution.

$$inf_{w.r.t.\ H,G} \left(\int_{[z,s]} c([z\ s\ ], [H(z)\ G(z,s)\ ])\ \ dp([z\ s\ ]) \right) + \lambda \left(\int_{z} c(z, H(z))\ \ dp(z) \right) \tag{3}$$

Notice that in Proposition 1 each term in Eq. 3 looks similar to Monge's formulation of optimal transport but without the boundary condition on the push forward function, and instead with the summation constraint of Eq. 2 on $H(.)$ and $G(.,.)$. Proof and a more formal statement of Proposition 1 is provided in Supplementary Note 2.

The connection between flow matching with mini-batches and the global optimal transport plan is not completely understood[68], and our method likewise is not guaranteed to find the optimal solution of Eq. 3. Nevertheless by introducing the flow matching objective we expect the marginal vector field to remain relatively simple[69] and remain somewhat close to optimal for the objective of Eq. 3. To this end, we add the following objectives:

$Objective_5$: $bi - directional\ flow\ matching\ objective\ on\ the\ mapping\ [z, s] \mapsto \left[\bar{x}^{int}, \bar{x}^{mic}\right]$

$Objective_6$: $bi - directional\ flow\ matching\ objective\ on\ the\ mapping\ z \mapsto \bar{x}^{int}$.

The above discussion sums up the rationale behind the objective terms considered, in addition to the usual evidence lower-bound (ELBO) terms, and describes why the proposed model is expected to be identifiable. However, to further encourage separation of intrinsic and spatial signals, we consider two additional objectives:

$Objective_7$: $MCC\ of\ a\ cell\ not\ being\ predictable\ from\ its\ z\ vector.$

$Objective_8$: $MCC\ of\ a\ cell\ not\ being\ predictable\ from\ its\ \bar{x}^{int}\ vector.$

The above objectives are induced by the discretized version of MCC, meaning from z or $\bar{x}^{int}$ of a cell a predictor cannot tell if it resides next to any specific cell type. This is in line with the basic intuition that the internal state of a cell does not contain information about the type of neighboring cells. $Objective_7$ and $Objective_8$ are implemented by Wasserstein distance distribution matching[70,71]. More precisely, for each cell type population, there is a cell type-specific discriminator (or dual function in the sense of Wasserstein distance estimation) that takes in z or $\bar{x}^{int}$ of a cell in the population and predicts if it resides in the neighborhood of any cell of that cell type assigned to the cell type-specific discriminator. In other words, if there are $|cell\ type|$-many cell types, we consider $|cell\ type| \times |cell\ type|$-many discriminators or dual functions where the fist $|cell\ type|$ multiplicand is pertinent to the number of populations per cell type and the second $|cell\ type|$ multiplicand corresponds to each MCC vector dimension. To reduce the amount of computation, we consider $|cell\ type|$ MLP backbones each having $|cell\ type|$-many output heads. We implemented Wasserstein distribution matching similar to Gulrajani *et al*[71].

Finally, as a standard modeling assumption[72], we encourage the intrinsic embeddings and expression components of cells with the same cell type label to be close. This is done via a mean squared loss for each pair of cells in the subgraph returned by PyTorch Geometric's neighbor loader and for their intrinsic embeddings and expression components:

$Objective_9$: $z\ vector\ of\ cells\ with\ the\ same\ cell\ type\ label\ being\ close.$

$Objective_{10}$: $\bar{x}^{int}\ vector\ of\ cells\ with\ the\ same\ cell\ type\ label\ being\ close.$

$Objective_{11}$: $x^{int}\ vector\ of\ cells\ with\ the\ same\ cell\ type\ label\ being\ close.$

Scalability

We now describe how our proposed MintFlow method achieves scalability (the details of the encoder/decoder formulation and architectures are provided in Supplementary Notes 3 and 4). The main hurdle towards scalability is that representations are interleaved via the spatial neighborhood graph; In the generative model (Supplementary Fig. 14a) it happens because the s^{out} vectors are averaged among neighbours, and on the inference side (Supplementary Fig. 14b) it happens because a graph neural network (GNN) decomposes the gene expression vector x_n of the n-th cell given those of its neighbors, to arrive at x_n^{int} and x_n^{mic}.

To solve this issue we adopted inductive graph learning which enables learning GNNs with subsampled subgraphs rather than processing the entire graph as its whole[73]. Given a GNN with k-hop receptive field, a selected subgraph has two sets of nodes: (1) central nodes for

whom all nodes in the k-hop neighborhood (testing phase) or a subset of neighbors in 1-, 2-, 3-, ..., and k- hop are present in the subgraph. (2) non-central nodes whose role is to provide to the GNN the context around the central nodes, so it can compute reliable values for them. In other words, GNN's output for the central nodes is valid and, e.g., a graph node classification loss can be computed from them. But the GNN's output for non-central nodes is not necessarily valid. This poses a challenge for MintFlow, because the vectors x^{int} and x^{mic} need to be computed for all cells in the subgraph (Supplementary Fig. 16a), including the central and non-central ones, from which the other vectors z, s^{in}, and s^{out} are computed for all cells. Doing so is necessary, because in the decoding phase all s^{out} vectors are needed, which in turn necessitates having x^{int} and x^{mic} for all cells. To alleviate this problem we resort to the probabilistic nature of the model; in the variational distribution we put a lower-bound on the predicted variance (i.e. uncertainty) for the x^{int} and x^{mic} vectors of non-central nodes to emphasize that those vectors are only some rough estimates by the encoder. Furthermore, we use the customized sampler described next.

We used PyTorch Geometric's neighbor loader[73] both for training and testing. The default sampler randomly selects some nodes (i.e. cells) as the central nodes and adds the k-hop neighbours to the subgraph. By doing so, non-central nodes (i.e. cells) may dominate the subgraph (Supplementary Fig. 16a). To tackle this issue we use a customized sampler that selects random crops from a tissue section (the blue squares in Supplementary Fig. 16b) as being the central nodes. Consequently, central nodes' neighbors are likely to be among central nodes, and non-central nodes are expected to reside on the boundaries of the selected crops (the red regions in Supplementary Fig. 16b). Thus, central nodes (i.e. cells) are expected to dominate the selected subgraph. Recall that - unlike the regular case of ,e.g., training a GNN node classifier - we need to use encoder predictions for both central and non-central nodes, hence in our use case the customized sampler is highly preferable. For efficient and scalable evaluation, we used the layered approach[74] in the testing phase.

Handling batch effect

MintFlow can be applied to a set of tissue sections with known or unknown technical or biological batch effects between them. To handle batch effects, the decoder modules for $\bar{x}^{int} \mapsto x^{int}$ and $\bar{x}^{mic} \mapsto x^{mic}$ as well as the first encoder module for $x \mapsto \left[x^{int}, x^{mic}\right]$ take in a one-hot encoded batch identifier. Furthermore, we implemented Wasserstein distribution matching similar to Gulrajani *et al*.[71] via two batch discriminators (or Wasserstein distance estimators) placed on top of $\bar{x}^{int}$ and $\bar{x}^{mic}$. Intuitively, in the model of Supplementary Fig. 14a, the variables z, s^{out}, s^{in}, $\bar{x}^{int}$, and $\bar{x}^{mic}$ are encouraged to be devoid of batch effects while x^{int} and x^{mic} are batch- and tissue section-dependant. For this reason, when running MintFlow on more than one tissue section with multiple batch identifiers, we use $\bar{x}^{int}$ and $\bar{x}^{mic}$ for different downstream

analyses like cell subpopulation identification. However, when MintFlow is run on a single tissue section one can use x^{int} and x^{mic}, e.g., after dimensionality reduction with PCA. There are two independently-tunable coefficients for batch mixing loss terms of $\bar{x}^{int}$ and $\bar{x}^{mic}$ whereby one can unequally encourage the batch mixing objectives on these embeddings. For example, one may want to encourage batch mixing mostly on $\bar{x}^{int}$ rather than $\bar{x}^{mic}$, and this can be done by setting the aforementioned two loss term coefficients to proper values.

Annealing the reconstruction loss

In our proposed model there are two latent vectors x^{int} and x^{mic} with as many dimensions as the number of genes (Supplementary Fig. 14a), and this causes complications, because two encoder/decoder architectures are needed: one for $\left[x^{int} \mapsto \bar{x}^{int} \mapsto x^{int}\right]$ and one for $\left[x^{mic} \mapsto \bar{x}^{mic} \mapsto x^{mic}\right]$. In particular, the predicted x^{int} and x^{mic} vectors keep changing during training and the corresponding encoder/decoder have to adapt their parameters on the fly. Conversely, during training the encoder/decoder reconstruction losses discourage the variational distribution to freely modify the assignment of read counts to x^{int} and x^{mic}, because doing so increases the reconstruction loss of the encoder/decoder. To alleviate this issue, we anneal the reconstruction loss, starting from a small loss coefficient and increasing it linearly to a larger number as the training continues, and finally continuing the training for a number of epochs with the largest coefficient for reconstruction loss.

Computing the microenvironment score

We use the identified x^{int} and x^{mic} vectors to compute a per-cell microenvironment score, which for the n-th cell is computed as: $\frac{\sum_j x_{nj}^{mic}}{\sum_j x_{nj}^{mic} + \sum_j x_{nj}^{int}}$, where the j index enumerates genes. Intuitively, a higher microenvironment score means that a larger proportion of the cell's total count is predicted to be induced by microenvironment. Therefore, as shown in Fig. 1d, colocalized cells with high microenvironment scores are candidate signaling hotspots.

In silico tissue perturbation

After training, the generative model can generate expression data merely given cell type labels and the spatial neighborhood graph of cells (Supplementary Fig. 14a). Notably, the generative model generates microenvironment-induced and intrinsic components of expression as well as total expression generated as the sum of the two components. This enables *in silico* perturbation to a tissue region, generating expression data for pre- and post-perturbed tissue region, and finally observing how the generated expression vectors and their

microenvironment-induced and intrinsic components change between pre- and post-perturbed tissue. The *in silico* perturbation can arbitrarily change cell type labels and the spatial neighborhood graph. Nonetheless, in our experiments we picked a tissue crop from real data and either altered cell type labels or discarded subpopulations of cells of specific types. Afterwards, the neighborhood graph is recreated for the post-perturbed tissue based on spatial locations of cells.

Datasets

We used MintFlow to analyze spatial transcriptomics data from four datasets: a simulated dataset, newly generated atopic dermatitis, and ccRCC datasets, and publicly available data of cutaneous melanoma (Supplementary Note 6 for detailed description). All spatial data were profiled using the 10x Genomics Xenium in situ 5k-plex platform and, where specified, analyzed with matched single-cell or single-nucleus RNA-seq datasets for validation and annotation. All human samples were obtained with appropriate ethics approvals and informed consent.

Data generation and acquisition

Cutaneous melanoma data was previously published (Data Availability section). All other data was newly generated.

Simulated data. Simulated spatial data were generated using the NicheCompass simulation framework[7], and comprised 10,000 cells and 2,000 genes across eight spatial regions. In the experiments presented in Supplementary Fig. 3, we excluded regions with MCCs consisting of only one cell type, because this is a harder setting where the MCC and CT labels are the same in some tissue regions and thus the separation of intrinsic and microenvironment-induced effects is challenging (Methods, $Objective_1$ and $Objective_2$).

Atopic dermatitis. Five lesional and five non-lesional skin biopsies were obtained from adult patients with atopic dermatitis (REC EC00/128). Sections (10 μm) were prepared and profiled via Xenium-5k, with protein staining for segmentation and subsequent H&E imaging.

Clear cell renal carcinoma. One nephrectomy case (PD43284; REC 03/018) was profiled across four regions (three tumor cores, one tumor–normal interface) and used for MintFlow training. Two other nephrectomy cases (PD45814 and PD45816) were used for validation.

Tissue was processed via the Xenium pipeline as above.

Preprocessing and cell type annotation

Raw counts were filtered to exclude poor quality cells. Gene expression matrices were normalized before log transformation. Dimensionality reduction using PCA and kNN graph construction, and clustering using the Leiden algorithm, were performed for each dataset. For

annotation, we used a dataset-specific approach. For AD and ccRCC, we used scVI embeddings and Leiden clustering for annotation, guided by DEGs, spatial context, and validation via CellTypist and ScanVI[24,25]. Melanoma annotations followed 10x metadata and DEGs for each cell type.

MintFlow training and outputs

MintFlow was trained on each dataset using the parameters specified in Supplementary Table 1. Utilizing X^{mic}, datasets were clustered to resolve microenvironment-induced gene programs (MGPs), with marker gene identification using scanpy.tl.score_genes. These MGPs were projected onto external scRNA-seq datasets, including a cross-tissue human atlas[25] and a ccRCC atlas[49].

Cell-cell communication, drug repurposing analysis and metabolic profiling

For AD, CellPhoneDB v5[75] was used to analyze chemokine interactions in the T_DC domain. Drug2cell[26] was used to rank candidate therapies targeting MGPs. Gene set enrichment scores for GO biological processes were calculated using GSEApy. For ccRCC, cell-cell communication was imputed using LIANA+[76] in "rank aggregate" mode, incorporating multiple ligand–receptor prediction algorithms, including CellPhoneDB, NATMI and CellChat.

Survival analysis

For ccRCC, MintFlow-derived T cell MGPs were applied to TCGA bulk RNA-seq data (n = 606 patients), Kaplan–Meier survival curves were generated after stratifying patients by median SGP score using R packages survival and survminer.

Benchmarked methods

To benchmark SIMVI[10], we used the code from https://github.com/KlugerLab/SIMVI (retrieved on April 8th, 2025). We set the hyperparameters as recommended in the MERFISH MTG data tutorial and used embedding size 10. We used the implementation of MEFISTO[13] in MOFA python package[77] and with default parameters. As done in Dong *et al.*[10] we computed the median of scale factors computed by MEFISTO[13], picked the factors whose corresponding scale is higher than the median value, and considered the decoded cell by gene matrix as microenvironment-induced expression vector. The default embedding size of the proposed MintFlow is 100. Whenever comparing MintFlow to other baselines, we reduced the embedding size to 10 since some baselines have huge memory and computation requirements, and are not runnable with embedding size equal to 100. Nonetheless, for some datasets running baselines was not feasible even when their hyperparameters were carefully tuned. In those

cases we ran the proposed MintFlow with default hyperparameters. For MintFlow, we used slightly different settings in different analyses. For example, in the benchmarking of Fig. 1h (left and middle), we reduced the size of embeddings to 10, and in the ablation study of Supplementary Fig. 7 we reduced the number of epochs, thereby making it possible to run several experiments in a reasonable time. Our experiments' configuration files for MintFlow CLI (command-line interface) are available online: https://github.com/Lotfollahi-lab/mintflow-experiments

Metrics

For simulated data the ground truth intrinsic and microenvironment-induced expression matrices (i.e. ground truth x^{int} and x^{mic}) are available. Therefore we used common metrics to measure how close MintFlow's predicted x^{mic} was to the ground truth: MAE (mean absolute error), MSE (mean squared error), and EMD (earth mover's distance). We computed the MAE and MSE using numpy, and EMD using scipy.stats.wasserstein_distance.

For real spatial transcriptomics data no ground truth for the microenvironment-induced component of expression is available, thus we cannot use the MAE, MSE, and EMD metrics. Therefore we acquired a list of genes expected to be related to cell-cell signaling. Specifically, we processed and combined many databases gathered at https://github.com/LewisLabUCSD/Ligand-Receptor-Pairs[19]. In our list we included each gene of interacting complexes, whenever complexes were reported in each database. We consider any gene that appears in any database as a "signaling gene" and otherwise a "non-signaling gene". Intuitively, if a read count (*i.e.* one element of the observed cell by gene matrix) corresponds to a signaling gene, then MintFlow is expected to assign a higher proportion of it to x^{mic} relative to x^{int}. This criterion is used in Fig. 1h.

Ablation study on simulated data

To experimentally validate Proposition 1 and show the effect of the flow matching objective we conducted experiments on simulated data. We varied:

- The importance coefficient of the flow matching objectives (*i.e.* $Objective_5$ and $Objective_6$).
- The scale factor for the encoders of z and s^{out}. Note that when the scale becomes large, in the limit it resembles how bi-directional flow matching[68] would generate samples of $\left[z, s^{in}\right]$ from the based distribution.

The former and latter were varied between $\{0.01, 0.1, 0.2, 0.5, 1.0\}$ and $\{0.01, 0.1, 0.2, 0.5, 1.0\}$, respectively, and the metrics MSE, MAE, and EMD were computed for 3 random runs in each experiment (Supplementary Fig. 18). The first row shows the average of each metric over 3 different runs. The second row shows the boxplots for each anti-diagonal of the heatmaps.

Note that, unlike in the heatmaps, all 3 runs are included in the boxplots. For example "anti-diag 1" corresponds to row 1 and column 1 in the heatmaps (*i.e.* one element of the matrix), but since there are 3 runs the box of "anti-diag 1" in the boxplot contains 3 circles. In Supplementary Fig. 18 the third and fourth rows show the boxplots for each row and each column. According to rows 1 and 2, as both the encoder noise for $\left[z, s^{in}\right]$ and the coefficient of flow matching loss increase (*i.e.* the lower right section of the heatmaps), the MSE and MAE metrics (cols 1 and 2) and Wasserstein metrics for z and $\left[z, s^{in}\right]$ (cols 3 and 4) reduce. Recall that the Wasserstein metrics correspond to the terms in Eq. (3) in Proposition 1, hence these figures show that reducing those terms helps in identifying the latent intrinsic and microenvironment-induced expression components, as anticipated by Proposition 1.

Incremental application of AD *in silico* perturbations

We repeated the AD perturbations (Fig. 3b,e) but instead of perturbing all cells of interest at once, we incrementally deleted or changed cells of specific types and inspected the gene expression of cells whose microenvironment cell type composition (MCC) had changed from the initial unperturbed tissue. For the *in silico* perturbation of Treg depletion we recreated the neighborhood graph after each incremental deletion of Treg cells.

References

1. Rood, J. E., Maartens, A., Hupalowska, A., Teichmann, S. A. & Regev, A. Impact of the Human Cell Atlas on medicine. *Nat. Med.* **28**, 2486–2496 (2022).
2. Binnewies, M. *et al.* Understanding the tumor immune microenvironment (TIME) for effective therapy. *Nature Medicine* **24**, 541–550 (2018).
3. Ji, A. L. *et al.* Multimodal Analysis of Composition and Spatial Architecture in Human Squamous Cell Carcinoma. *Cell* **182**, 497–514.e22 (2020).
4. Fiskin, E. *et al.* Multi-modal skin atlas identifies a multicellular immune-stromal community associated with altered cornification and specific T cell expansion in atopic dermatitis. *bioRxiv* (2023) doi:10.1101/2023.10.29.563503.
5. Habib, N. *et al.* Disease-associated astrocytes in Alzheimer's disease and aging. *Nat Neurosci* **23**, 701–706 (2020).
6. Fischer, D. S., Schaar, A. C. & Theis, F. J. Modeling intercellular communication in tissues using spatial graphs of cells. *Nat. Biotechnol.* **41**, 332–336 (2023).
7. Birk, S. *et al.* Quantitative characterization of cell niches in spatially resolved omics data. *Nat. Genet.* (2025) doi:10.1038/s41588-025-02120-6.
8. Singhal, V. *et al.* BANKSY unifies cell typing and tissue domain segmentation for scalable spatial omics data analysis. *Nat. Genet.* (2024) doi:10.1038/s41588-024-01664-3.
9. Varrone, M., Tavernari, D., Santamaria-Martínez, A., Walsh, L. A. & Ciriello, G. CellCharter reveals spatial cell niches associated with tissue remodeling and cell plasticity. *Nat. Genet.*

56, 74–84 (2024).
10. Dong, M., Su, D. G., Kluger, H., Fan, R. & Kluger, Y. SIMVI disentangles intrinsic and spatial-induced cellular states in spatial omics data. *Nat. Commun.* **16**, 2990 (2025).
11. Levy, N., Ingelfinger, F., Ergen-Behr, C. & Nadler, B. Nichevi: A probabilistic framework to embed cellular interaction in spatial transcriptomics. (2024).
12. Jerby-Arnon, L. & Regev, A. DIALOGUE maps multicellular programs in tissue from single-cell or spatial transcriptomics data. *Nature Biotechnology* **40**, 1467–1477 (2022).
13. Velten, B. *et al.* Identifying temporal and spatial patterns of variation from multimodal data using MEFISTO. *Nat. Methods* **19**, 179–186 (2022).
14. Townes, F. W. & Engelhardt, B. E. Nonnegative spatial factorization applied to spatial genomics. *Nat. Methods* **20**, 229–238 (2023).
15. Chen, S., Regev, A., Condon, A. & Ding, J. CellUntangler: separating distinct biological signals in single-cell data with deep generative models. *bioRxiv* (2025) doi:10.1101/2025.01.10.632490.
16. Efremova, M., Vento-Tormo, M., Teichmann, S. A. & Vento-Tormo, R. CellPhoneDB: inferring cell-cell communication from combined expression of multi-subunit ligand-receptor complexes. *Nat. Protoc.* **15**, 1484–1506 (2020).
17. Jin, S. *et al.* Inference and analysis of cell-cell communication using CellChat. *Nat. Commun.* **12**, 1088 (2021).
18. Wolf, F. A., Angerer, P. & Theis, F. J. SCANPY: large-scale single-cell gene expression data analysis. *Genome Biol.* **19**, 15 (2018).
19. Armingol, E., Officer, A., Harismendy, O. & Lewis, N. E. Deciphering cell-cell interactions and communication from gene expression. *Nat. Rev. Genet.* **22**, 71–88 (2021).
20. Morrison, V. L. *et al.* The β2 integrin-kindlin-3 interaction is essential for T-cell homing but dispensable for T-cell activation in vivo. *Blood* **122**, 1428–1436 (2013).
21. Montoya, M. C. *et al.* Role of ICAM-3 in the initial interaction of T lymphocytes and APCs. *Nat. Immunol.* **3**, 159–168 (2002).
22. Gérard, A., Cope, A. P., Kemper, C., Alon, R. & Köchl, R. LFA-1 in T cell priming, differentiation, and effector functions. *Trends Immunol.* **42**, 706–722 (2021).
23. Jin, H. *et al.* IL-21R is essential for epicutaneous sensitization and allergic skin inflammation in humans and mice. *J. Clin. Invest.* **119**, 47–60 (2009).
24. Reynolds, G. *et al.* Developmental cell programs are co-opted in inflammatory skin disease. *Science* **371**, eaba6500 (2021).
25. Steele, L. *et al.* A single cell and spatial genomics atlas of human skin fibroblasts in health and disease. *bioRxiv* 2024.12.23.629194 (2024) doi:10.1101/2024.12.23.629194.
26. Kanemaru, K. *et al.* Spatially resolved multiomics of human cardiac niches. *Nature* **619**, 801–810 (2023).
27. Bachert, C. *et al.* Biologics for chronic rhinosinusitis with nasal polyps. *J. Allergy Clin. Immunol.* **145**, 725–739 (2020).
28. Han, Y. *et al.* Amlexanox exerts anti-inflammatory actions by targeting phosphodiesterase

4B in lipopolysaccharide-activated macrophages. *Biochim. Biophys. Acta Mol. Cell Res.* **1867**, 118766 (2020).
29. Weidinger, S., Beck, L. A., Bieber, T., Kabashima, K. & Irvine, A. D. Atopic dermatitis. *Nat. Rev. Dis. Primers* **4**, 1 (2018).
30. Kato, A. & Kita, H. The immunology of asthma and chronic rhinosinusitis. *Nat. Rev. Immunol.* 1–19 (2025).
31. Pitzalis, C., Jones, G. W., Bombardieri, M. & Jones, S. A. Ectopic lymphoid-like structures in infection, cancer and autoimmunity. *Nat. Rev. Immunol.* **14**, 447–462 (2014).
32. Migayron, L., Merhi, R., Seneschal, J. & Boniface, K. Resident memory T cells in nonlesional skin and healed lesions of patients with chronic inflammatory diseases: Appearances can be deceptive. *J. Allergy Clin. Immunol.* **153**, 606–614 (2024).
33. Obers, A. *et al.* Retinoic acid and TGF-β orchestrate organ-specific programs of tissue residency. *Immunity* **57**, 2615–2633.e10 (2024).
34. Reina-Campos, M. *et al.* Tissue-resident memory CD8 T cell diversity is spatiotemporally imprinted. *Nature* 1–10 (2025).
35. Osaki, M. & Sakaguchi, S. Soluble CTLA-4 regulates immune homeostasis and promotes resolution of inflammation by suppressing type 1 but allowing type 2 immunity. *Immunity* **58**, 889–908.e13 (2025).
36. Bluestone, J. A. *et al.* Regulatory T cell therapies to treat autoimmune diseases and transplant rejection. *Nat. Immunol.* **26**, 819–824 (2025).
37. Liu, J., Zhang, X., Cheng, Y. & Cao, X. Dendritic cell migration in inflammation and immunity. *Cell. Mol. Immunol.* **18**, 2461–2471 (2021).
38. Ho, P. *et al.* Harnessing regulatory T cells to establish immune tolerance. *Sci. Transl. Med.* **16**, eadm8859 (2024).
39. Moon, C. Y. *et al.* Dendritic cell maturation in cancer. *Nat. Rev. Cancer* **25**, 225–248 (2025).
40. Wang, W. *et al.* Single-cell profiling identifies mechanisms of inflammatory heterogeneity in chronic rhinosinusitis. *Nat. Immunol.* **23**, 1484–1494 (2022).
41. Rapp, M. *et al.* CCL22 controls immunity by promoting regulatory T cell communication with dendritic cells in lymph nodes. *J. Exp. Med.* **216**, 1170–1181 (2019).
42. Arpinati, L., Carradori, G. & Scherz-Shouval, R. CAF-induced physical constraints controlling T cell state and localization in solid tumours. *Nat. Rev. Cancer* **24**, 676–693 (2024).
43. Preview Data: FFPE Human Skin Primary Dermal Melanoma with 5K Human Pan Tissue and Pathways Panel. *10x Genomics* https://www.10xgenomics.com/datasets/xenium-prime-ffpe-human-skin.
44. Gao, Y. *et al.* Cross-tissue human fibroblast atlas reveals myofibroblast subtypes with distinct roles in immune modulation. *Cancer Cell* **0**, (2024).
45. Sangaletti, S. *et al.* Mesenchymal transition of high-grade breast carcinomas depends on extracellular matrix control of myeloid suppressor cell activity. *Cell Rep.* **17**, 233–248 (2016).

46. Murdamoothoo, D. *et al.* Tenascin-C immobilizes infiltrating T lymphocytes through CXCL12 promoting breast cancer progression. *EMBO Mol. Med.* **13**, e13270 (2021).
47. Yamauchi, M., Barker, T. H., Gibbons, D. L. & Kurie, J. M. The fibrotic tumor stroma. *J. Clin. Invest.* **128**, 16–25 (2018).
48. Chhabra, Y. & Weeraratna, A. T. Fibroblasts in cancer: Unity in heterogeneity. *Cell* **186**, 1580–1609 (2023).
49. Li, R. *et al.* Mapping single-cell transcriptomes in the intra-tumoral and associated territories of kidney cancer. *Cancer Cell* **40**, 1583–1599.e10 (2022).
50. Masuda, T. *et al.* Unique characteristics of tertiary lymphoid structures in kidney clear cell carcinoma: prognostic outcome and comparison with bladder cancer. *J. Immunother. Cancer* **10**, e003883 (2022).
51. Xu, W. *et al.* Heterogeneity in tertiary lymphoid structures predicts distinct prognosis and immune microenvironment characterizations of clear cell renal cell carcinoma. *J. Immunother. Cancer* **11**, e006667 (2023).
52. Meylan, M. *et al.* Tertiary lymphoid structures generate and propagate anti-tumor antibody-producing plasma cells in renal cell cancer. *Immunity* **55**, 527–541.e5 (2022).
53. Teillaud, J.-L., Houel, A., Panouillot, M., Riffard, C. & Dieu-Nosjean, M.-C. Tertiary lymphoid structures in anticancer immunity. *Nat. Rev. Cancer* **24**, 629–646 (2024).
54. Pichler, R. *et al.* A chemokine network of T cell exhaustion and metabolic reprogramming in renal cell carcinoma. *Front. Immunol.* **14**, 1095195 (2023).
55. Braun, D. A. Progressive immune dysfunction with advancing disease stage in renal cell carcinoma Cancer Cell. **39**, 632–648.
56. Cheuk, S. *et al.* CD49a expression defines tissue-resident CD8+ T cells poised for cytotoxic function in human skin. *Immunity* **46**, 287–300 (2017).
57. Matos, T. R. *et al.* Clinically resolved psoriatic lesions contain psoriasis-specific IL-17-producing αβ T cell clones. *J. Clin. Invest.* **127**, 4031–4041 (2017).
58. Jingushi, K. *et al.* Leukocyte-associated immunoglobulin-like receptor 1 promotes tumorigenesis in RCC. *Oncol. Rep.* **41**, 1293–1303 (2019).
59. Kato, R. *et al.* TIM3 expression on tumor cells predicts response to anti-PD-1 therapy for renal cancer. *Transl. Oncol.* **14**, 100918 (2021).
60. ClinicalTrials.gov. https://clinicaltrials.gov/study/NCT06546553?cond=Kidney%20Cancer&term=LILRB1&rank=1.
61. Rombach, R., Blattmann, A., Lorenz, D., Esser, P. & Ommer, B. High-resolution image synthesis with latent diffusion models. *arXiv [cs.CV]* (2021).
62. Chen, R. T. Q., Rubanova, Y., Bettencourt, J. & Duvenaud, D. Neural ordinary differential equations. *arXiv [cs.LG]* (2018).
63. Hyvärinen, A. & Pajunen, P. Nonlinear independent component analysis: Existence and uniqueness results. *Neural Netw.* **12**, 429–439 (1999).
64. Khemakhem, I., Kingma, D., Monti, R. & Hyvarinen, A. Variational Autoencoders and

Nonlinear ICA: A Unifying Framework. in *Proceedings of the Twenty Third International Conference on Artificial Intelligence and Statistics* (eds. Chiappa, S. & Calandra, R.) vol. 108 2207–2217 (PMLR, 26--28 Aug 2020).

65. Lachapelle, S. *et al.* Disentanglement via Mechanism Sparsity Regularization: A New Principle for Nonlinear ICA. in *Proceedings of the First Conference on Causal Learning and Reasoning* (eds. Schölkopf, B., Uhler, C. & Zhang, K.) vol. 177 428–484 (PMLR, 11--13 Apr 2022).
66. Moran, G. E., Sridhar, D., Wang, Y. & Blei, D. M. Identifiable deep generative models via sparse decoding. *arXiv [stat.ML]* (2021).
67. Lopez, R. *et al.* Learning Causal Representations of Single Cells via Sparse Mechanism Shift Modeling. in *Proceedings of the Second Conference on Causal Learning and Reasoning* (eds. van der Schaar, M., Zhang, C. & Janzing, D.) vol. 213 662–691 (PMLR, 11--14 Apr 2023).
68. Tong, A. *et al.* Improving and generalizing flow-based generative models with minibatch optimal transport. *arXiv [cs.LG]* (2023).
69. Lipman, Y., Chen, R. T. Q., Ben-Hamu, H., Nickel, M. & Le, M. Flow Matching for generative modeling. *Int Conf Learn Represent* **abs/2210.02747**, (2022).
70. Arjovsky, M., Chintala, S. & Bottou, L. Wasserstein Generative Adversarial Networks. *ICML* **70**, 214–223 (2017).
71. Gulrajani, I., Ahmed, F., Arjovsky, M., Dumoulin, V. & Courville, A. C. Improved Training of Wasserstein GANs. *Neural Inf Process Syst* **30**, 5767–5777 (2017).
72. Kleshchevnikov, V. *et al.* Cell2location maps fine-grained cell types in spatial transcriptomics. *Nat. Biotechnol.* **40**, 661–671 (2022).
73. Hamilton, W. L., Ying, R. & Leskovec, J. Inductive representation learning on large graphs. *arXiv [cs.SI]* (2017).
74. Yin, P. *et al.* DGI: An easy and efficient framework for GNN model evaluation. in *Proceedings of the 29th ACM SIGKDD Conference on Knowledge Discovery and Data Mining* 5439–5450 (ACM, New York, NY, USA, 2023).
75. Vento-Tormo, R. *et al.* Single-cell reconstruction of the early maternal-fetal interface in humans. *Nature* **563**, 347–353 (2018).
76. Dimitrov, D. *et al.* LIANA+ provides an all-in-one framework for cell-cell communication inference. *Nat. Cell Biol.* **26**, 1613–1622 (2024).
77. Argelaguet, R. *et al.* MOFA+: a statistical framework for comprehensive integration of multi-modal single-cell data. *Genome Biol.* **21**, 111 (2020).